1
Introduction

1.1
Graphene-Based Nanomaterials

Carbon exists in many forms including buckyballs, diamond, nanotubes, and graphite. It is naturally abundant as coal and natural graphite. Two-dimensional (2D) graphene, a new class of carbon nanostructure, has attracted tremendous attention in recent years since the successful isolation of graphene by micromechanical cleavage of highly oriented pyrolytic graphite (HOPG) [1, 2]. Graphene is a single atomic layer of sp^2 hybridized carbon atoms covalently bonded in a honeycomb lattice. It is a building block for carbon materials of different dimensionalities, including 0D buckyballs, 1D nanotubes, and 3D graphite (Figure 1.1). It shows great potential for technological applications in several areas such as electronics, optoelectronics, nanocomposites, sensors, batteries, and so on [3–7]. Graphene sheets stack together to form graphite with an interlayer spacing of 0.34 nm, showing strong in-plane bonding but weak van der Waals interaction between layers. By virtue of this layered structure, large efforts have been tempted to exfoliate graphite into individual atomic layers. It is difficult to obtain a fully separated sheet layer of graphene because freestanding atomic layer is widely considered to be thermodynamically unstable. A lack of an effective approach to exfoliate graphite into individual, pure graphene sheet in large quantities remains a major obstacle to exploiting its full potential applications.

In 2004, Geim and coworkers of the Manchester University (United Kingdom) prepared single layer of graphene using the cohesive tape method through repeated peeling of graphite and deposited onto a Si/SiO_2 substrate [1, 2]. This is often referred to as a *scotch tape* or *drawing method*. Optical microscopy was initially used to distinguish individual graphene layers followed by their identification in an atomic force microscope (AFM). Geim and Novoselov received the Nobel Prize in Physics for 2010 for their pioneering work in the fabrication and physical characterization of graphene. Such novel preparation of graphene has opened up a new era in nanotechnology and materials science and prompted much excitement in these fields. This technique can only produce low-yield, high-purity graphene for research purposes, and insufficient for practical applications. Moreover, it is hard to control the number of layers for peeled off pieces.

Polymer Composites with Carbonaceous Nanofillers: Properties and Applications, First Edition. Sie Chin Tjong.

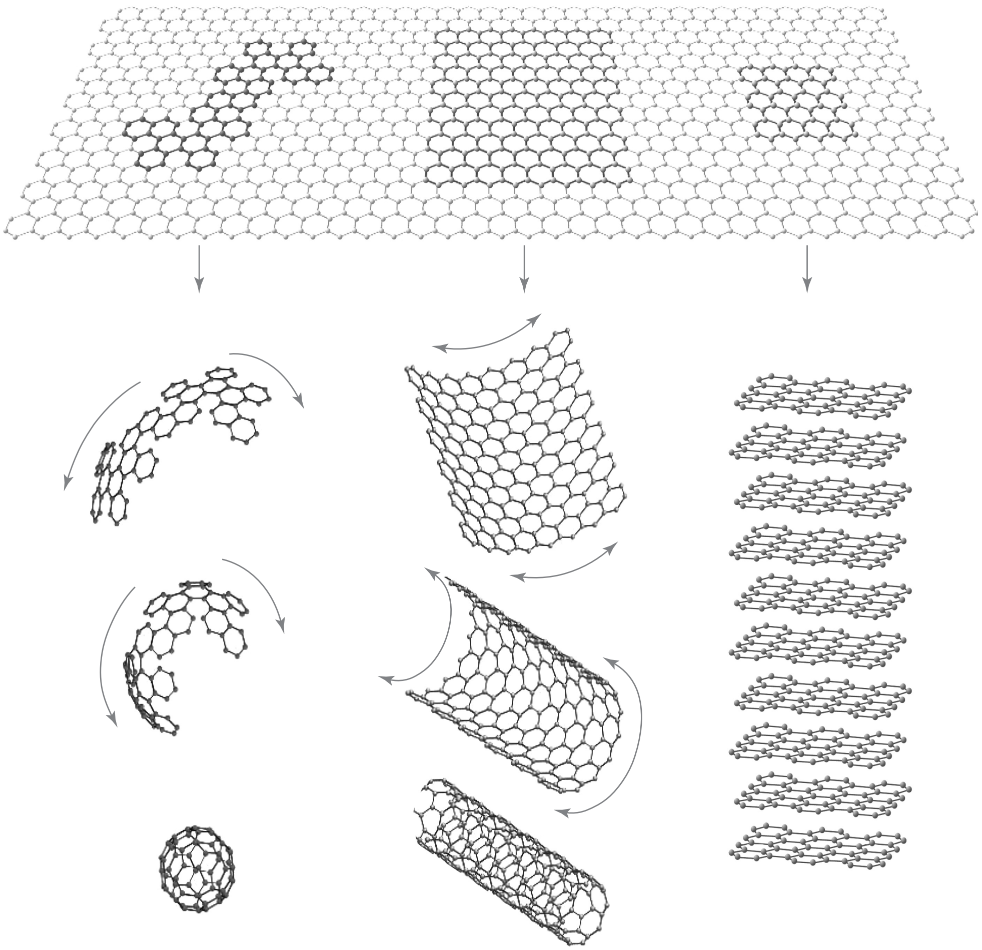

Figure 1.1 Graphene is a 2D building material for carbon materials of different dimensionalities. It can be wrapped up into 0D buckyballs, rolled into 1D nanotubes, or stacked into 3D graphite. (Source: Reproduced with permission from Ref. [3], Nature Publishing Group (2007).)

As an alternative, graphene can be grown directly on solid substrates using two different approaches. The first involves graphitization of single-crystal silicon carbide substrate through thermal desorption of silicon in ultrahigh vacuum at high temperatures (circa above 1300 °C). Consequently, excess carbon is left behind on the surface. The carbon-enriched surface then undergoes reorganization and graphitization to form graphene under proper control sublimation conditions. This process yields epitaxial graphene with dimensions dependant on the size of SiC substrate [8, 9]. The shortcomings of this process are the use of high processing temperature, the formation of atomic scale defects in the graphene lattice and the difficulty of achieving large graphite domains with uniform thickness. The second approach involves epitaxial growth of graphene on metal carbide (e.g., TaC, TiC) or metallic substrates (e.g., Ni, Cu) via chemical vapor deposition (CVD) of hydrocarbons at high temperatures. This is commonly followed by chemical etching and transfer printing to arbitrary substrates [10–14]. For example, Kim *et al.* [11] prepared patterned graphene film on thin nickel layer using a gas mixture of CH_4, H_2, and Ar, followed by transferring the printing film onto target substrates. The growth of graphene on nickel with higher carbon solubility (>0.1 at%) occurs by the diffusion of the carbon species into the metal surface before segregating and precipitating to the surface on fast cooling. Ni can dissolve more carbon atoms and thus it is difficult to obtain uniform graphene films due to precipitation of extra C during fast cooling. In contrast, the graphene growth on low carbon solubility Cu substrates occurs by means of surface adsorption process [13]. CVD graphene generally exhibits lower electron mobility than mechanically exfoliated graphene because of its higher concentration of point defects, smaller grain sizes, and residual impurities from the transfer or growth processes [14]. The transfer-printing process is also difficult to scale up for industrial applications. Accordingly, wet chemical processing through oxidation of graphite into graphene oxide (GO) followed by reduction appears to be a cost-effective method for mass-producing graphenelike materials.

1.1.1
Graphite Intercalation Compound

Apparently, high-yield production processes for graphene sheets are necessary for practical applications as conductive films and nanofillers for composite materials. Hence, chemical conversion from graphite offers significant advantages over physical approaches and the CVD process for preparing graphene for large-scale applications. This approach converts natural graphite into graphite intercalation compound (GIC) by reacting with electron-donor agents such as alkali metals and electron-acceptor agents such as halogens and acids [15]. Because of its layered structure, acid molecules and alkali metal can penetrate within the gallery spaces of graphite. The layers of graphite interact with the guest molecules through charge transfer process. For example, potassium can be inserted into graphite galleries to yield both first stage and higher stages of intercalation. Stage implies the number of graphite host layers divided by the number of guest layers that occur periodically in the galleries. In the case where every carbon layer in graphite is intercalated, a stage I compound forms, while intercalating on average every other layer yields a stage II compound [16a]. The first-stage intercalation compound, KC_8, has a larger d-spacing (0.541 nm) compared to that of graphite. The second-stage compound, KC_{24}, and the third-stage material, KC_{36}, have a spacing of 0.872 and 1.2 nm, respectively (Figure 1.2). KC_8 generally forms by heating graphite with potassium under vacuum at 200 °C [16b]. The KC_8 compound then reacts with ethanol to yield potassium ethoxide and hydrogen gas, which aid in separating the graphitic sheets

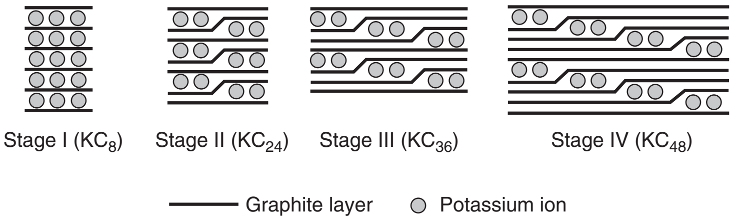

Figure 1.2 Schematic diagram of graphite host layers intercalated with different numbers of potassium guest layers. (Source: Reproduced with permission from [16a], Elsevier (2007).)

to form exfoliated graphite. The reaction takes place as follows:

$$KC_8 + CH_3CH_2OH \rightarrow 8C + KOCH_2CH_3 + \tfrac{1}{2}H_2 \tag{1.1}$$

Apart from potassium, the intercalate species normally employed for forming GICs include sulfuric acid, perchloric acid, and selenic acid. In the former case, sulfuric species intercalates into the gallery spaces of graphite in the presence of oxidizing nitric acid. The chemical reaction that takes place between graphite and concentrated sulfuric acid is given by Chen *et al.* [17a,b]

$$n(\text{graphite}) + nH_2SO_4 + n/2[O] \rightarrow n[\text{graphite} \cdot HSO_4] + n/2\,H_2O \tag{1.2}$$

where O is the oxidant and graphite · HSO_4 is the GIC.

Expanded graphite (EG) is an industrial term for exfoliated graphite obtained from sulfuric acid-based GIC precursor [18]. Rapid heating or microwave irradiation causes a large expansion of the graphite flakes along their *c*-axis to produce EGs of ~50–400 nm thickness. In general, microwave heating is more effective to exfoliate GIC than conventional thermal treatment because of its high-energy density and fast heating process. Microwave heating vaporizes the acids within the layers of graphite, producing a significant and rapid expansion of the graphite gallery [19]. Figure 1.3a,b shows the low- and high-magnification scanning electron micrographs showing typical porous, vermicular, or wormlike morphology of EGs. The EGs can be further exfoliated to graphite nanoplatelets (GNPs) of 1–15 μm in diameter and a thickness of <10 nm under sonication in the solvents [17b, 20]. The morphology of individual GNP particle is shown in Figure 1.4a,b. The term *nanoplatelet* describes the formation of several layers of graphene rather than a single graphene layer.

1.1.2
Graphene Oxide

Graphite oxide can be obtained by reacting graphite with strong oxidizers such as sulfuric acid, nitric acid, potassium chlorate, and potassium permanganate. The typical Staudenmaier [21] oxidation method involves a mixture of sulfuric acid, nitric acid and potassium chlorate. The Hummers process involves chemical oxidation of graphite with $KMnO_4$ and $NaNO_3$ in concentrated H_2SO_4 [22]. Till

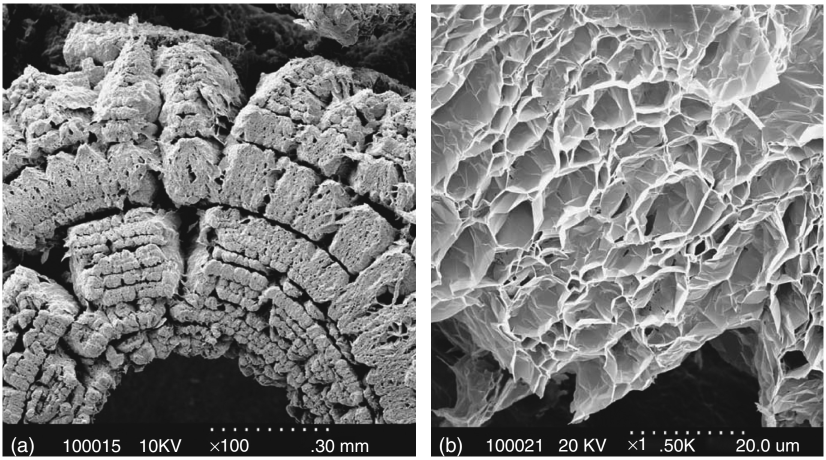

Figure 1.3 (a) SEM image of EGs showing wormlike morphology. (b) High-magnification SEM image showing pores intersperse with EG platelets. (Source: Reproduced with permission from Ref. [18], Elsevier (2005).)

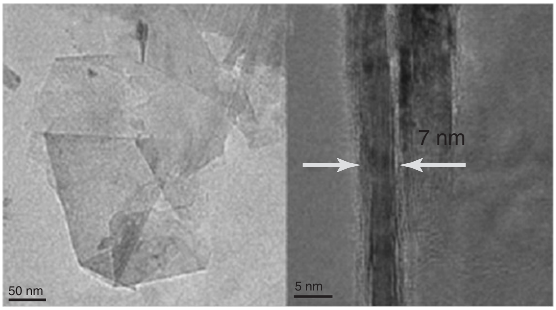

Figure 1.4 TEM images of (a) surface and (b) cross-sectional view of an individual graphite nanoplatelet particle. (Source: Reproduced with permission from Ref. [20], Elsevier (2011).)

present, this is the most commonly used process. Graphite oxide is decorated with hydrophilic oxygenated graphene sheets bearing oxygen functional groups on their basal planes and edges [23, 24]. In other words, functional groups such as epoxide, hydroxyl, carbonyl, and carboxyl groups are formed in the basal planes (Figure 1.5). Thus graphite oxide exhibits an increased interlayer spacing from original 3.4 Å of graphite to 6.0–10 Å nm depending on the water content [25]. Such functional groups make graphite oxide hydrophilic and weaken the van der Waals forces between layers. Thus graphite oxides can be dispersed in aqueous media readily to form colloidal suspensions [26]. This facilitates exfoliation of graphite oxide into GO sheets via sonication [27]. Figure 1.6 is an AFM image of GO exfoliated in water via sonication showing the presence of sheets with uniform thickness of $\sim$1 nm. This thickness is somewhat larger than the theoretical value of 0.34 nm found in

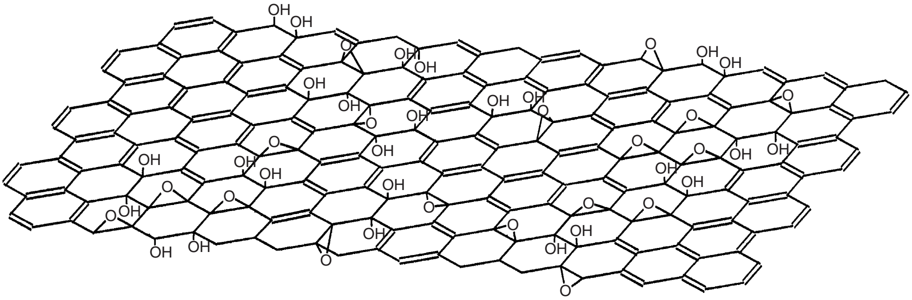

Figure 1.5 Chemical structure of graphite oxide. Carboxylic groups at the edges are not shown. (Source: Reproduced with permission from [24a], Elsevier (1998).)

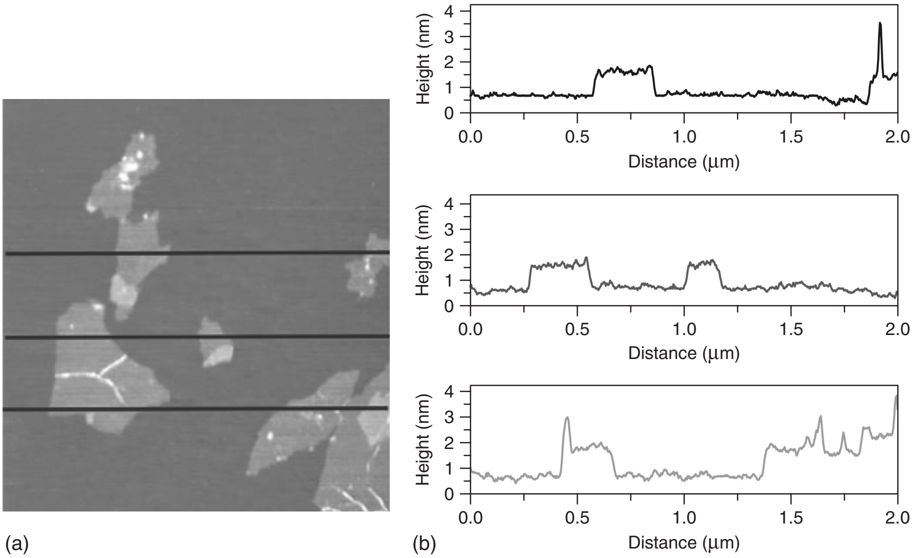

Figure 1.6 (a) AFM image of exfoliated graphene oxide sheets. The sheets are ~1 nm thick. The horizontal lines in the image indicate the sections (in order from top to bottom) corresponding to the height profiles shown (b). (Source: Reproduced with permission from Ref. [27], Elsevier (2007).)

graphite. This is attributed to the presence of covalently bound oxygen in the GO. It appears that large-scale production of graphene sheets can be achieved through chemical oxidation and exfoliation of graphite flakes in the liquid phase, and the subsequent deoxygenation reduction owing to its simplicity, reliability, and low material cost.

GO is electrically insulating because the functional groups distort intrinsic network of the sp^2 carbon–carbon bonds in the graphene sheets. To recover electrical conductivity, chemical reducing agents such as hydrazine and its derivatives have been used to eliminate oxygen functionalities. For example, Ruoff and coworkers added hydrazine hydrate directly to aqueous dispersions of GO to remove epoxide complexes, producing reduced graphene oxide (rGO), and often referred to as chemically modified graphene (CMG) [25, 28]. A possible reaction pathway for epoxide reduction is given by Stankovich *et al.* [27]

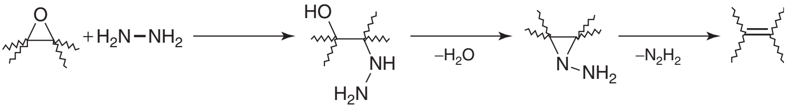

(1.3)

It is noted that hydrazine (N_2H_4) is highly toxic and the treatment causes the formation of unsaturated and conjugated carbon atoms, which in turn degrades electrical conductivity. Residual carbonyl and carboxyl groups still can be found in the C1s X-ray photoelectron spectroscopy (XPS) spectrum because of incomplete chemical reduction by hydrazine (Figure 1.7). Further, C−N groups are also incorporated during chemical reduction. The residual oxygen forms sp^3 bonds with carbon atoms in the basal plane such that the carbon sp^2 bonding fraction in fully reduced GO is ~0.8 [29]. Very recently, Shin *et al.* [30] reported that sodium borohydride ($NaBH_4$) is more effective to remove oxygen moieties in GO than hydrazine. Nevertheless, rGO shows promise for technological applications since it can be processed in liquid phase in large quantities, thus facilitating the fabrication of thin films and composites using low-cost solution processing techniques [28, 31]. Figure 1.8 outlines the process scheme for fabricating rGO-based films for polymer composite and graphene-related electronics applications.

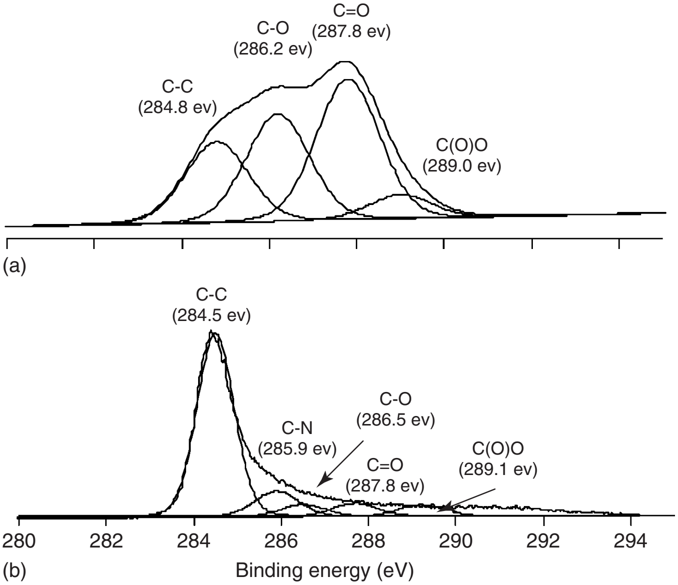

Figure 1.7 C1s spectra of (a) GO and (b) reduced GO. (Source: Reproduced with permission from Ref. [27], Elsevier (2007).)

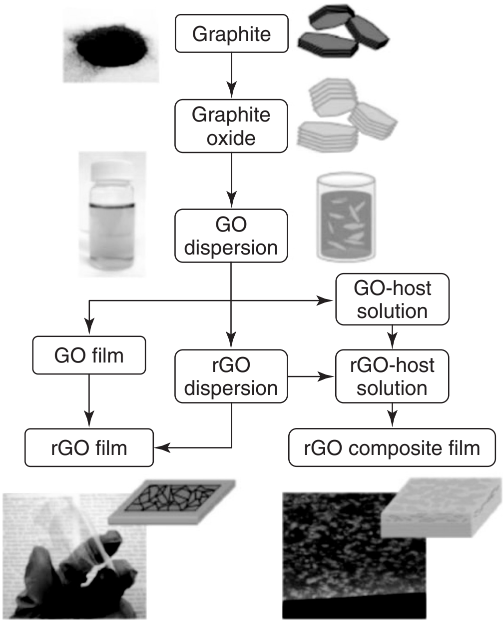

Figure 1.8 Process scheme for fabricating rGO-based thin films. (Source: Reproduced with permission from Ref. [28], Wiley-VCH (2010).)

In addition to chemical reduction, large quantities of graphene can be obtained by reducing GO thermally. This involves rapidly heating GO in an inert atmosphere to form thermally reduced graphene oxide (TRG) or thermally expanded graphene oxide (TEGO). Aksay and coworkers [32a,b] reduced GO by rapid heating ($>2000\,^{\circ}\mathrm{C\,min^{-1}}$) to 1050 °C, resulting in the evolution of carbon dioxide due to the decomposition of hydroxyl and epoxide groups. The evolved gas pressure

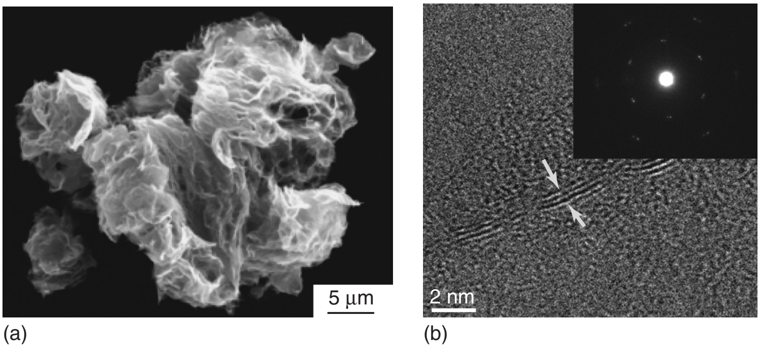

Figure 1.9 (a) SEM image of dry FGS powder. (Source: Reproduced with permission from Ref. [32b], the American Chemical Society (2007).) (b) HRTEM image of TEGO. The inset is selected-electron diffraction pattern of TEGO. (Source: Reproduced with permission from Ref. [33], the American Chemical Society (2009).)

then increases, forcing the sheets apart and producing exfoliation of graphene sheets. TEGO is also known as functionalized graphene sheet (FGS) having a wrinkled morphology (Figure 1.9a). Some functional groups are still retained despite high-temperature annealing. High-resolution transmission electron microscopy (HRTEM) image of TEGO reveals the presence of approximately three to four individual graphene layers within the platelet [33] (Figure 1.9b). Erickson *et al.* [34] investigated the local chemical structures rGO and TEGO films using a transmission electron microscopy (TEM) corrected with monochromatic aberration. GO was produced using a modified Hummers method and drop cast into TEM carbon grids. GO-containing grids were reduced in a hydrazine atmosphere and then slowly heated to 550 °C under flowing nitrogen to form TEGO. The TEM image of GO obviously shows the presence of the oxidized areas (A and B) and graphene region (C) (Figure 1.10). The TEM image of TEGO reveals a high amount of

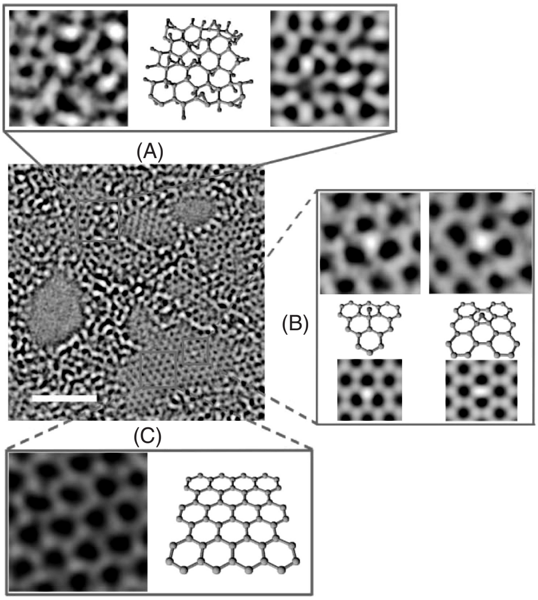

Figure 1.10 Aberration-corrected TEM image of a single sheet of suspended GO. The scale bar is 2 nm. Expansion (A) shows, from left to right, a 1 nm^2 enlarged oxidized region of the material, then a proposed possible atomic structure of this region with carbon atoms in gray and oxygen atoms in dark gray, and finally the average of a simulated TEM image of the proposed structure and a simulated TEM image of another structure where the position of oxidative functionalities has been changed. Expansion (B) focuses on the white spot on the graphitic region. This spot moved along the graphitic region but stayed stationary for three frames (6 s) at a hydroxyl position (left portion of expansion (B)) and for seven frames (14 s) at a (1,2) epoxy position (right portion of expansion (B)). The ball-and-stick figures below the microscopy images represent the proposed atomic structure for such functionalities. Expansion (C) shows a 1 nm^2 graphitic portion from the exit plane wave reconstruction of a focal series of GO and the atomic structure of this region. (Source: Reproduced with permission from Ref. [34], Wiley-VCH (2010).)

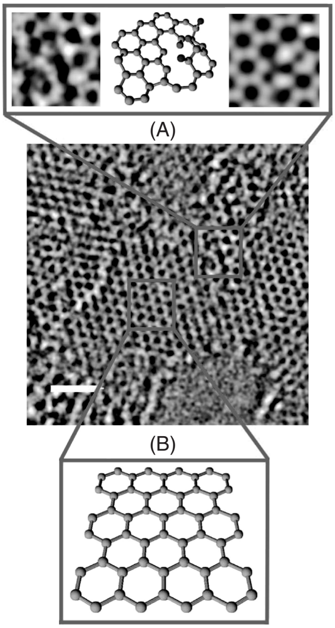

Figure 1.11 Aberration-corrected TEM image of a monolayer of TEGO. The scale bar is 1 nm. Expansion (A) shows, from left to right, an enlarged region of the micrograph, then a proposed possible structure for the region and finally a simulated TEM image for this proposed structure. Expansion (B) shows the structure of a graphitic region. (Source: Reproduced with permission from Ref. [34], Wiley-VCH (2010).)

restored graphene area (B) with little oxidized area (A) associated with oxygenated functional groups (Figure 1.11).

1.2
Carbon Nanotubes

Since the documented discovery of carbon nanotubes (CNTs) by Iijima in 1991, the properties and potential applications of CNTs have attracted considerable interests among scientific and technological communities. This is because one-dimensional CNTs exhibit large aspect ratio, exceptionally high tensile strength and modulus, as well as excellent electrical and thermal conductivity. Single-walled carbon nanotube (SWNT) consists of a single graphene layer rolled up into a seamless cylinder. Thus CNT is also composed of a network with the sp^2 carbon–carbon bonds. The nanotube structure is typically characterized by a chiral vector ($\vec{C}_h$) defined by the relation: $\vec{C}_h = n\vec{a}_1 + m\vec{a}2$ where $\vec{a}_1$ and $\vec{a}_2$ are the graphene lattice vectors and n and m are integers. The chiral vector determines the direction along which the graphene sheets are rolled up to form nanotubes (Figure 1.12). The electronic properties of SWNTs are highly sensitive to the variations in diameter and the indices of

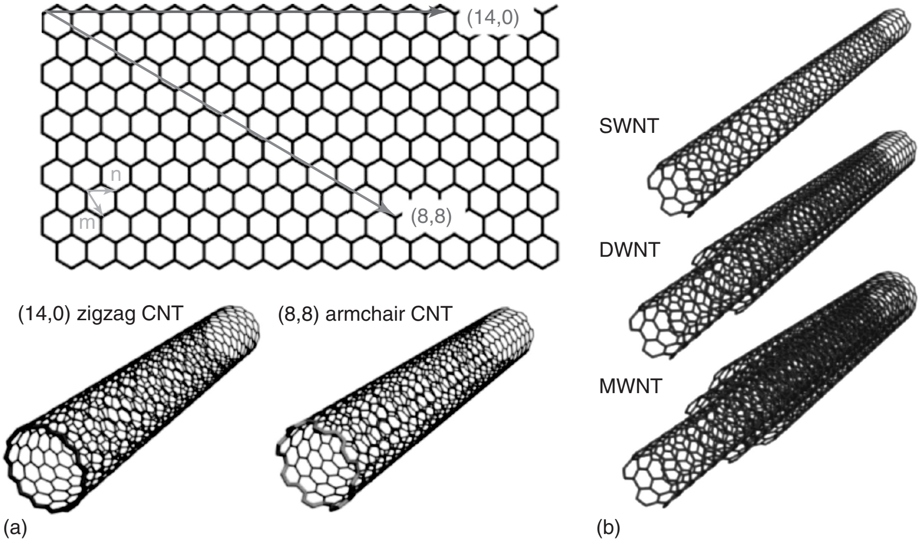

Figure 1.12 Structural variety of CNTs. (a) Orientation of the carbon network in armchair (*n*,*n*) and zigzag (*n*,0) CNTs. (b) Single-, double-, and multiwalled CNTs. (Source: Reproduced with permission from Ref. [36], the American Chemical Society (2011).)

their chiral vector, n and m [35, 36]. Armchair nanotubes ($n = m$) generally show metallic conducting behavior, while zigzag ($m = 0$) or chiral ($n \neq m$) CNTs are semiconducting. Double-walled and multiwalled carbon nanotubes (MWNTs) are composed of two and several graphene layers wrapped onto concentric cylinders with an interlayer spacing of 0.34 nm. The diameters of CNTs range from a few for SWNTs to several nanometers for MWNTs.

1.2.1
Synthesis of Carbon Nanotubes

1.2.1.1 Physical Vapor Deposition

CNTs have been synthesized by a variety of physical vapor deposition (PVD) and CVD processes. Both processes have their advantages and disadvantages for synthesizing nanotubes. PVD can be classified into direct current (DC) arc discharge and the laser ablation. Those involve condensation of hot carbon vapor generated by evaporating solid graphite. In the former method, an arc is formed between two high-purity graphite electrodes under a protective atmosphere of inert gases. The carbon vapor then condenses on the cold cathode forming a cigarlike deposit with a hard outer shell and a softer inner core [37]. CNTs are then deposited in the weblike soot attached on the chamber walls or electrodes [38]. This technique generally favors the formation of CNTs with a higher degree of crystallinity and structural integrity because of the high temperature of arc plasma. However, by-products such as amorphous carbon and other carbonaceous species are also generated. The quality and yield of nanotubes depend on the processing

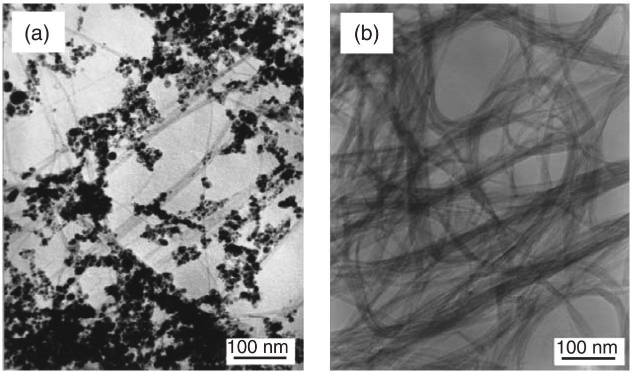

Figure 1.13 TEM images of (a) arc-grown SWNTs in H_2 and (b) purified SWNTs. (Source: Reproduced with permission from Ref. [41], Elsevier (2008).)

conditions such as efficient cooling of cathode, the gap between electrodes, reaction chamber pressure, uniformity of the plasma arc, plasma temperature, and so on. [39]. Comparedto laser ablation, electric arc discharge technique is cheaper and easier to implement but has lower output yield.

SWNTs can also be synthesized by the arc discharge evaporation of a carbon electrode with the aid of transition metal catalyst in hydrogen-containing environments such as H_2–inert gas (Ne, Ar, Kr, and Xe) or H_2–N_2 [40]. The as-prepared SWNT soot generally contains a large amount of impurities including transition metal catalysts, amorphous carbon, and carbonaceous particle impurities, rendering purification of the arc-SWNTs a big challenge [41] (Figure 1.13). Ando and coworkers [42, 43] demonstrated that the arc discharge of pure graphite in pure hydrogen results in the formation of MWNTs of high crystallinity in the cathode deposit.

Laser ablation refers to removal of substantial amount of material from the target by an intense laser pulse. In the process, a graphite target placed inside a tube furnace is irradiated with a focused laser beam. A stream of inert gas is admitted into the specimen chamber for carrying vaporized species downstream to a cold finger [44] (Figure 1.14). The Nd:YAG and CO_2 laser sources operated in a continuous wave mode are typically used for generating carbon vapor species. The quality and yield of CNTs can be manipulated by several experimental parameters including the composition of the target, gas atmosphere, pressure and its flow rate, as well as the laser energy, peak power, and repetition rate [38, 45–48]. SWNTs synthesized from this process often assemble into bundles because of the van der Waals attractions between them [49]. Figure 1.15a,b shows the respective TEM images of SWNTs produced by vaporizing a graphite target containing Pt, Rh, and Re catalysts at 1450 °C in nitrogen or helium gas atmospheres with a laser source [48]. SWNT bundles and amorphous carbon can be readily seen in these micrographs. However, the amount of amorphous carbon is relatively higher in the SWNTs synthesized in helium.

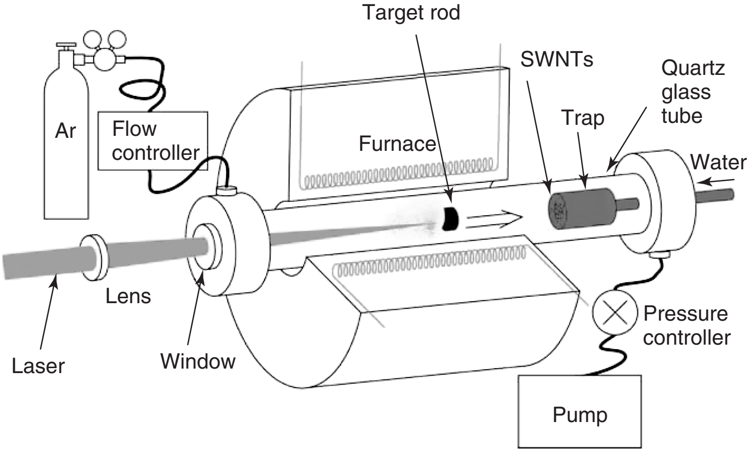

Figure 1.14 Laser ablation facility for synthesizing CNTs. (Source: Reproduced with permission from Ref. [44], Elsevier (2004).)

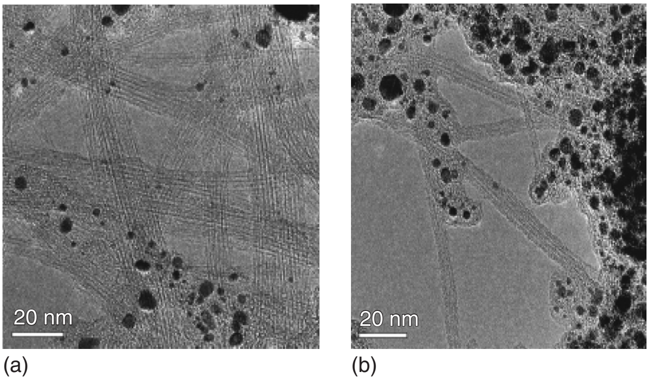

Figure 1.15 TEM images of SWNTs synthesized from a graphite target containing Pt, Rh, and Re catalysts by a Nd:YAG laser irradiation at 1450 °C in (a) nitrogen and (b) helium. (Source: Reproduced with permission from Ref. [48], the American Chemical Society (2007).)

1.2.1.2 **Chemical Vapor Deposition**

CVD method is a versatile and effective technique for massive synthesis of CNTs at low production cost using a wide variety of hydrocarbon gases such as methane, ethylene, propylene, acetylene, and so on. It allows the manufacture of CNTs into various forms including thin films, aligned, or entangled tubes as well as free-standing nanotubes. The process involves catalytic dissociation of hydrocarbon gases over metal nanoparticle catalysts in a high-temperature reactor. Comparing with the arc-grown CNTs, CVD-synthesized nanotubes generally have higher density of structural defects. The types of CNTs produced depend mainly on the synthesis temperatures. MWNTs are generally formed at ~600–850 °C, while SWNTs are produced at higher temperatures of 900–1200 °C [44]. CVD can be classified into two categories, that is, thermal- and plasma-enhanced processes depending on the heating sources employed. Thermal CVD decomposes hydrocarbon gases using thermal energy. The hydrocarbon precursor is usually diluted with H_2, normally acting as carrier gases [50, 51].

The catalytic decomposition of hydrocarbons can be further enhanced by using plasmas generated from DC, hot filament aided with DC, microwave, radio frequency (rf), electron cyclotron resonance (ECR), and inductively coupled plasma sources. These sources ionize the gas precursors, producing plasmas, electrons, ions, and excited radical species. The setup of DC plasma reactor is relatively simple and consists of a couple of electrodes with one grounded and the other connecting to a power supply. The negative DC bias applied to the cathode causes the decomposition of hydrocarbon gases. To enhance deposition efficiency, a metallic wire (e.g., tungsten) is added to the system as resistively heated hot filament [52]. This is known as the *DC-plasma*-enhanced hot filament CVD [53], typically used for depositing diamond and diamondlike films. However, the DC plasma is less effective in producing reactive species since the majority of energy consumed in DC plasmas is lost in accelerating ions in the sheath, and this leads to a substantial substrate heating [52]. The plasma instability of DC reactors has led to the adoption of high-frequency plasma reactors in the semiconductor industry. In high-frequency plasma reactors, the gas molecules are activated by electron impact. For example, a microwave source operated at a frequency at 2.45 GHz at 1.5–2 kW oscillates electrons effectively, leading to an increase in their density (Figure 1.16a). These electrons then collide with the feed gas to form radicals and ions. In general, the ECR source is capable of producing higher fluxes of lowenergy ions than other sources (Figure 1.16b). It is well known that electrons travel in a circular path with a cyclotron frequency under the influence of a magnetic field. The cyclotron frequency is proportional to the strength of magnetic field. Electrons that move in a circular path in a magnetic field can absorb energy from an AC electric field provided that the frequency of the field matches the cyclotron frequency. In the ECR reactor, microwaves are introduced into a volume of the reactor at a frequency matches closely with ECR. The absorbed energy then increases the velocity of electrons, leading to enhanced ionization of the feed gas. Thus ECR source has the advantages of obtaining high dissociation levels of the precursor gas and high uniformity of plasma energy distribution.

Plasma-enhanced chemical vapor deposition (PECVD) allows nanotubes to be synthesized at lower temperatures [54–56]. It also offers another advantage by forming vertically aligned nanotubes over a large area with superior uniformity in diameter and length by means of the electric field present in the plasma sheath [57–60]. PECVD process is more complicated than thermal CVD since several plasma parameters such as ion density, ion energy, radical species, radical densities, and applied substrate bias are involved [61]. Since the dissociation of hydrocarbon feedstock creates many reactive radicals, leading to the deposition of amorphous carbon on the substrate. It is necessary to dilute the hydrocarbon with hydrogen, argon, or ammonia. The chemistry of gas precursors is considered of primarily

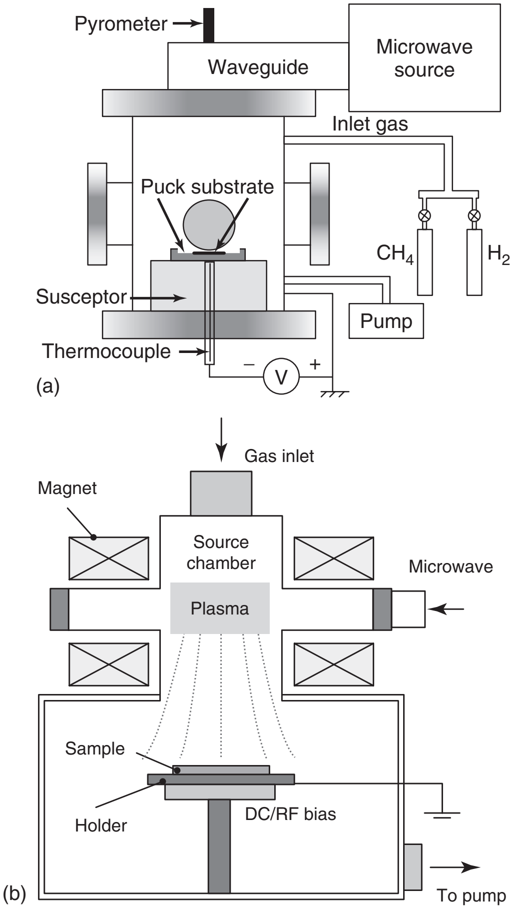

Figure 1.16 Schematic diagrams of (a) microwave PECVD and (b) ECR PECVD reactors. (Source: Reproduced with permission from Refs. [54] and [55], Elsevier (2006) and (2007), respectively.)

importance for growing aligned nanotubes. The hydrogen gas generally assists the growth of aligned nanotubes by etching the substrate. Atomic hydrogen generated within the plasma can remove amorphous carbon deposit on the substrate [62]. Figure 1.17a,b shows the respective low- and high-magnification scanning electron micrographs of aligned CNT film grown on a cobalt-catalyzed Si substrate using microwave PECVD [60]. However, Wong *et al.* [63] demonstrated that ammonia gas is even more effective to form aligned CNTs from microwave PECVD process. This is because ammonia can inhibit the formation of amorphous carbon during the initial synthesis stage [64].

The growth of CNTs during CVD process involves two main step sequences, that is, dissolution of the gas precursors into carbon atoms on the metal catalyst surface and surface diffusion of carbon atoms to the growth site to form the nanotube.

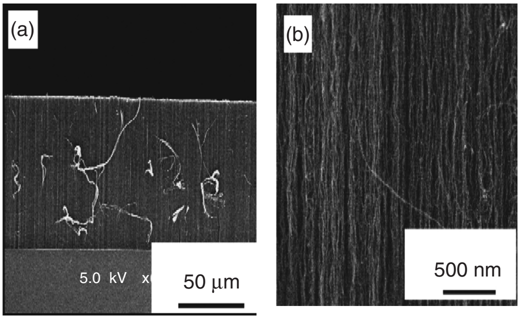

Figure 1.17 (a) Low- and (b) high-magnification scanning electron micrographs of aligned CNT film grown on a Co-catalyzed Si substrate using mixed CH_4-H_2 gases. (Source: Reproduced with permission from Ref. [60], Elsevier (2007).)

At an earlier stage of the process, catalytic dissociation of hydrocarbon molecules occurs near metal nanoparticles. Carbon atoms then absorb and diffuse on the metal surfaces, forming liquid alloy droplets. The droplets act as preferential sites for further adsorption of the carbon atoms, forming metal carbide clusters [65]. When the clusters reach supersaturation, nucleation, and preferential growth of 1D carbon nanostructure takes place [66]. This growth behavior is commonly known as the vapor-liquid-solid (VLS) mechanism [67]. Further, the growth can initiate either below or above the metal catalyst, regarding as the ''base'' or ''tip'' growth models (Figure 1.18). The former growth mode occurs assuming the presence of a strong metal catalyst-substrate interaction. Thus the nanotube grows up in 1D manner with the catalyst particle pinned on the substrate surface. In the case of a weak catalyst-substrate interaction, the catalyst particle is lifted up by the growing nanotube and encapsulated at the nanotube tip eventually. There is a speculation

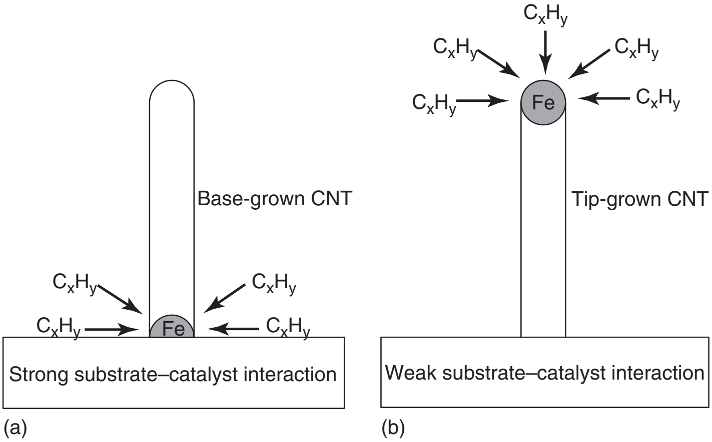

Figure 1.18 (a,b) ''Base'' and ''tip'' growth models for CNTs. (Source: Reproduced with permission from Ref. [44], Elsevier (2004).)

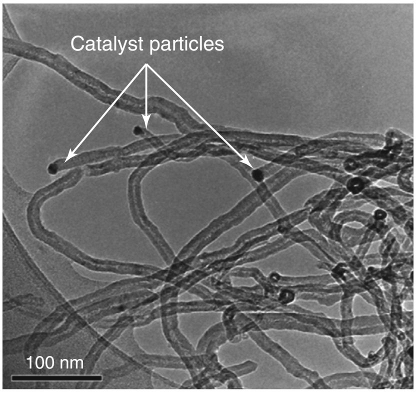

Figure 1.19 TEM image of CVD MWNTs synthesized using Ni-Al catalyst at 550 °C. (Source: Reproduced with permission from Ref. [68], Elsevier (2008).)

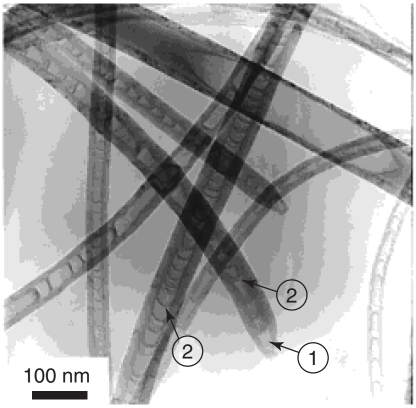

Figure 1.20 TEM image of CNTs grown at 850 °C. CNTs exhibit a bamboolike structure. The arrow 1 indicates the closed tip with no encapsulated Fe particle. The arrow 2 corresponds to the compartment layers whose curvature is directed to the tip. (Source: Reproduced with permission from Ref. [69], the American Chemical Society (2001).)

that MWNTs follow the "top" growth mode, while SWNTs adopt the "base" growth fashion [61]. Figure 1.19 is a TEM image showing the presence of nickel-aluminum composite catalysts at the tips of CVD MWNTs [68].

Park and Lee [69] synthesized CNTs using thermal CVD on a Fe-catalyzed silica substrate using C_2H_2 gas from 550 to 950 °C. They reported that CNTs grown at 950, 850, 750, and 600 °C exhibit a bamboolike morphology. There are no encapsulated Fe particles at the closed tips (Figure 1.20). The CNTs grown at 550 °C possess encapsulated Fe particles at the closed tips. Accordingly, they proposed propose a base growth model for the bambootype CNTs (Figure 1.21a–e). Carbons produced from the decomposition of C_2H_2 adsorb on the catalytic metal particle. They then diffuse on the metal particle surface to form the graphitic sheet cap (Figure 1.21a).

As the cap grows up from the catalytic particle, a closed tip with a hollow tube is produced (Figure 1.18b). The compartment graphite sheets are then formed on the inner surface of the catalyst due to carbon accumulation as a result of bulk diffusion (Figure 1.21c). The growth process continues progressively, forming a bambootype CNT (Figure 1.21d,e). Similarly, Chen *et al.* also reported that the CNTs deposited on Ni-catalyzed Si substrate via hot-filament CVD also follow the base growth mode. Figure 1.22a clearly shows the presence of encapsulated Ni particles at the nanotube end-substrate interface. The nanotubes also exhibit a bamboolike morphology. A high-resolution transmission electron micrograph reveals that the Ni particle exhibits a conical morphology (Figure 1.22b). The bamboolike feature of the nanotubes is also apparent.

Apart from the hydrocarbon feedstock, carbon monoxide is an alternative carbon source gas for synthesizing CNTs. The research group at Rice University developed and commercialized high-pressure carbon oxide disproportionation (HiPCo) process for synthesizing SWNTs using carbon monoxide and iron pentacarbonyl ($Fe(CO)_5$) catalyst [71]. This process enables the production of a relatively high yield of SWNTs. The nanotubes are synthesized in a flowing CO reactor at temperatures of 800–1200 °C under high pressures of 1–10 atm. On heating, the $Fe(CO)_5$ decomposes into Fe atoms that condense into larger nanoparticles. SWNTs then nucleate and grow on these particles in the gas phase via CO disproportionation (decomposition into C and CO_2) reaction

$$CO + CO \rightarrow CO_2 + C\ (SWNT) \tag{1.4}$$

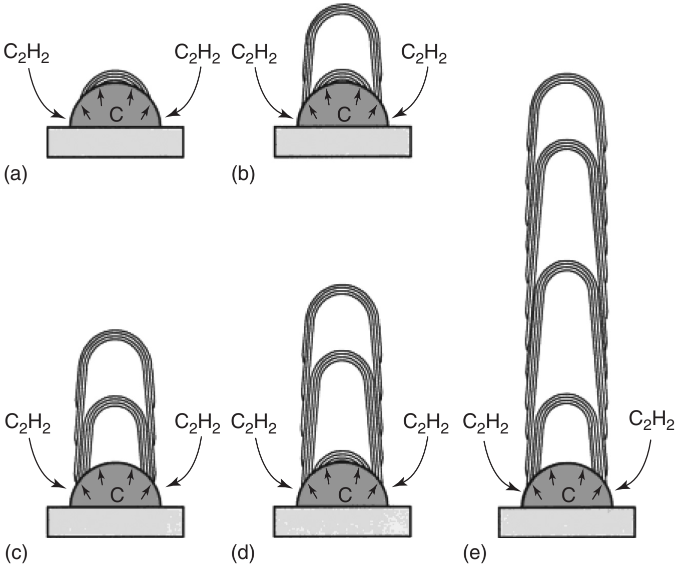

Figure 1.21 Schematic diagrams of a base growth model. (Source: Reproduced with permission from Ref. [69], the American Chemical Society (2001).)

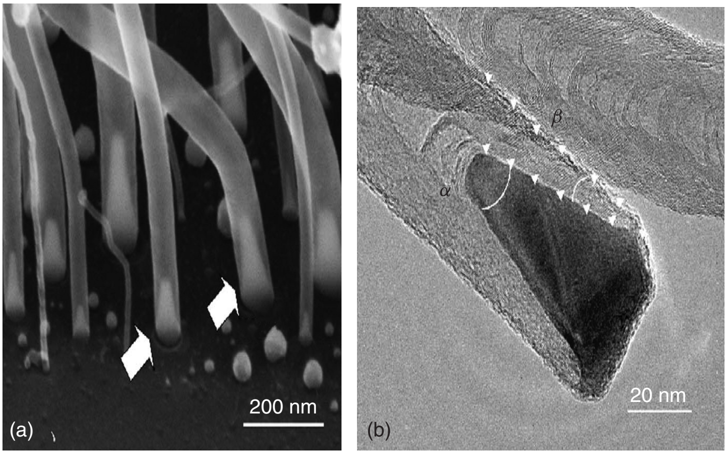

Figure 1.22 (a) SEM and (b) HRTEM images of CNTs grown on the Ni film/silicon substrate in a C_2H_4/NH_3 atmosphere using hot-filament CVD process. Conical-shape nickel nanoparticles are marked with arrows in (a). (Source: Reproduced with permission from Ref. [70], Elsevier (2004).)

1.2.2
Purification of Carbon Nanotubes

The as-synthesized CNTs generally contain a large amount of impurities including metal catalyst particles, amorphous carbon, fullerenes, and multishell graphitic carbon. For example, arc discharge nanotubes possess a considerable content of amorphous carbon, fullerenes, and carbon enclosing metal catalyst particles. The SWNTs synthesized from the CVD process contain metallic catalyst and amorphous carbon. These impurities affect electrical, mechanical, and biological properties of the CNTs markedly. Thus they must be removed before their practical applications in biomedical engineering and industrial sectors. Because of the diversity of the nanotube synthesis techniques, the as-prepared CNTs may have different morphologies, structures, and impurity levels. Thus the purification techniques must be properly tailored and selected to obtain CNTs with desired purity. It is a challenging task to effectively purify CNTs without damaging their structures. The purification routes can be classified into chemical- and physical-based techniques. The former includes gas- and liquid-phase oxidation, while the latter includes filtration, centrifugation, high-temperature annealing, and chromatography. The most widely adopted purification process is the liquid-phase oxidation because of their simplicity and capability for the removal of metal impurities to a certain concentration level. However, such process often results in structural damages to the nanotubes because of their vulnerability to chemical oxidation.

1.2.2.1 Chemical Techniques

Gas-phase oxidation is the simplest technique for purifying CNTs by removing carbonaceous impurities. It is ineffective to remove metal catalyst particles [41].

Accordingly, this method is suitable for purifying arc-grown MWNTs containing no metal catalysts. CNTs can be oxidized in air, pure oxygen, or chlorine atmosphere at a temperature range of 300–600 °C. The oxidants breach the carbon shell and then oxidize metal catalysts into metal oxides. As the oxidation proceeds, the volume of nanotube increases, and metal oxides crack open the carbon shell surroundings accordingly [72]. Carbonaceous impurities are oxidized at a faster rate than the nanotube material via selective oxidation [73]. The main disadvantage of thermal oxidation is that the process can burn off more than 95% of the nanotube material. This leads to an extremely low purification yield [74]. Alternatively, microwave heating has been found to be an effective method to purify arc-grown SWNTs because of its short processing time. The microwave induces rapid local heating of the catalyst particles, causing both the oxidation and rupture of the carbon layer surrounding metal catalyst particles [74].

In general, thermal oxidation is ineffective for the purification of SWNTs having large tube curvatures and metallic impurities. Additional step procedure is necessary for removing metal catalysts. Smalley and coworkers [75] developed the oxidation and deactivation of metal oxides for purifying raw HiPCo SWNTs. The metal oxides formed in the SWNTs by oxygen oxidation were deactivated into metal fluorides through reacting with $C_2H_2F_4$, SF_4, and other fluorine-containing gases [75]. As a result, the iron content was significantly decreased from ∼30 to ∼1 wt% with ∼70% SWNT yield. This purification process is mainly designed for the HiPCo SWNTs with predominant Fe particles. The toxicity of the reagents is another issue that must be considered from using this process.

Liquid-phase oxidation involves the use of oxidizing agents such as concentrated HNO_3, mixed HNO_3/H_2SO_4 (1 : 3 by volume), HCl, $KMnO_4$, $HClO_4$, and H_2O_2 for purifying the nanotubes, followed by the filtering and drying procedures. Strong oxidants such as $KMnO_4$ and $HClO_4$ are mainly used for the purification of MWNTs with higher resistance to oxidation. Nitric acid is found to be fairly effective in removing metal catalysts and amorphous carbon in the arc-grown SWNTs [76]. In general, a mixed HNO_3/H_2SO_4 (1 : 3 by volume) solution is more effective than concentrated nitric acid in removing impurities [77]. Thus this solution is widely used for the liquid-phase oxidation of CNTs today. As nitric acid is a mild reducing agent, a prolonged oxidation time of up to 50 h is needed to eliminate metallic impurities of the arc-grown SWNTs to a level below 0.2% [76] (Table 1.1). This produces significant wall damages, length reduction, and losses of the nanotube materials. In this regard, a two-step (e.g., gas-phase thermal oxidation followed by dipping in acid) process is adopted for further eliminating metallic component of the arc-grown SWNTs. For a combined thermal and acid oxidation treatment, the acid can easily dissolve the metal oxides formed from the gaseous oxidation. Table 1.1 compares metal content of the arc-grown SWNTs containing Ni and Y catalysts before and after purifying by nitric acid, air oxidation/HNO_3 reflux, and microwave heating/HCl reflux treatments. Apparently, an initial oxidation of the SWNTs in air at 400 °C for 30 min can reduce the refluxing time in a nitric acid to 6 h to yield a residual metal content $<1\%$. In contrast, microwave heating in air at 500 °C for 20 min followed by refluxing in HCl for 6 h can further remove residual

Table 1.1 Residual metal contents in Arc-Grown SWNTs containing Ni and Y impurities purified by different approaches.

Sample	Purification treatments	Metal content (wt%)	Comments (based on high-resolution transmission electron microscopy)
SWNTs	As-prepared	~35	SWNTs and metal residue covered by amorphous and multishell carbon
	Reflux HNO_3 acid at 130 °C for 25 h	~4	Significant wall damages and shorten tubes, losses of SWNTs
	Reflux HNO_3 acid at 130 °C for 50 h	<0.2	Significant wall damages and shorten tubes, losses of SWNTs
	Oxidation in air at 400 °C for 30 min, then reflux HNO_3 for 6 h	<1	No amorphous carbon, wall damages, losses of SWNTs
	Microwave heating in air at 500 °C for 10 min, reflux HCl for 6 h	~1.5	Some amorphous carbon on the walls, metal residue covered by multishell carbon
	Microwave heating in air at 500 °C for 20 min, reflux HCl for 6 h	<0.2	Slight wall damages due to the metals attached to the tube's walls

Source: Reproduced with permission from Ref. [76], the American Chemical Society (2002).

metal catalyst content to a level below 0.2%. Hou *et al.* [41] used a reverse sequence strategy, that is, an initial sonication in ethanol followed by air oxidation to purify hydrogen arc-grown SWNTs. Sonication is recognized as one of the effective ways to eliminate amorphous impurities in CNTs using suitable solvents and acid [78, 79]. Using such a two-step procedure, a purity of about 96% with a 41% SWNT yield can be achieved (Figure 1.23b). However, sonication can also induce structural defects in CNTs including buckling and bending [80].

It is noteworthy that the acid treatment induces structural defects and shortens the lengths of both the MWNTs and SWNTs (Table 1.1). The treatment also disrupts and opens the ends of CNTs, thus introducing oxygenated functional groups (hydroxyl and carboxyl) on the nanotube surfaces. These functional groups degrade electrical conductivity of the nanotubes markedly. However, these are beneficial in improving the dispersion of nanotubes in the polymer matrix.

1.2.2.2 **Physical Techniques**

Physical-based purification is an alternative route to reduce the damage of CNTs caused by chemical oxidation. It can retain the intrinsic structure of CNTs that is highly desirable for scientific research purposes and technological applications, particularly for the device and sensor applications. Physical techniques are mainly based on the dispersion of nanotubes in a stable colloidal suspension by the size separation through filtration, centrifugation, or chromatography. CNTs generally exhibit poor dispersibility in polar media such as water and organic solvents. SWNTs often agglomerate into bundles and ropes [49]; thus surfactants are widely used to stabilize the nanotube suspensions in water. Insoluble CNTs of large aspect ratios are extracted from the suspensions through filtration. Bonard *et al.* [82] dispersed pristine MWNTs in water with sodium dodecyl sulfate (SDS), forming a stable colloidal suspension. The suspension was filtered through a funnel large enough to allow the insertion of an ultrasonic probe. In order to increase the separation yield, successive filtrations were carried out until the attainment of desired purity. Smalley and coworkers employed both the filtration and the microfiltration to purify SWNTs produced by pulsed laser ablation [83]. The process separates carbon nanospheres, metal nanoparticles, polyaromatic carbons and fullerenes from the SWNTs. Purity of SWNTs in excess of 90 wt% can be achieved. The disadvantage of this technique is the use of a number of successive filtration steps to achieve desired purity.

Centrifugation is based on the gravity effects to separate carbon nanoparticles, amorphous carbon from the nanotube suspension. Thus it involves the use of centrifugal force for sedimentation of the suspensions. Amorphous carbon can be removed from the nitric-acid-treated SWNTs by low-speed centrifugation (2000*g*) in an acid solution of pH 2, leaving the SWNTs in the sediment in an acid [84]. Carbon nanoparticles in the SWNTs can be eliminated by high-speed centrifugation (20 000*g*) of several cycles in a neutral pH. This leads to the sedimentation of carbon nanoparticles, leaving the SWNTs suspended in aqueous media [85]. In another study, centrifugation in the SDS aqueous solutions is found to be effective for the removal of carbonaceous impurities in the SWNTs [86]. In general, filtration and centrifugation can only remove carbonaceous impurities and ineffective for the elimination of metallic impurities.

High-temperature annealing is the only one physical technique that does not involve the use of colloidal solutions. This process can effectively remove residual metal impurities in the CNTs when compared with other purification techniques such as acid treatment, filtration, and centrifugation. As recognized, a trace amount of metallic impurities in the CNTs can induce inflammation and cell apoptosis in mammals. These impurities must be completely removed for biomedical engineering applications. The annealing process involves heat treatment of nanotubes at high temperatures ($>1400\,^{\circ}$C) under inert atmosphere or high vacuum [81, 87–90]. Andrews *et al.* [81] annealed MWNTs at temperatures between 1600 and 3000 °C. They reported that heat treatment of MWNTs at temperatures above 1800 °C is very effective to remove residual metals (Figure 1.23a,b). Furthermore, high-temperature annealing can induce graphitization, resulting in the appearance of high-order diffraction spots such as (004) and (006) reflections in the selected-area electron diffraction (SAED) pattern. High-temperature annealing converts disordered structure of the walls of MWNTs into a more perfect graphitic structure (Figure 1.24a–f). In general, high-temperature heating can induce structural changes in the CNTs [88]. A twofold increase in the diameter of SWNTs is observed by heating at 1500 °C under argon and hydrogen atmospheres [89]. Similarly, Yudasaka *et al.* [90] reported that the diameters of HiPCo SWNTs can be increased via heat treatments at 1000–2000 °C.

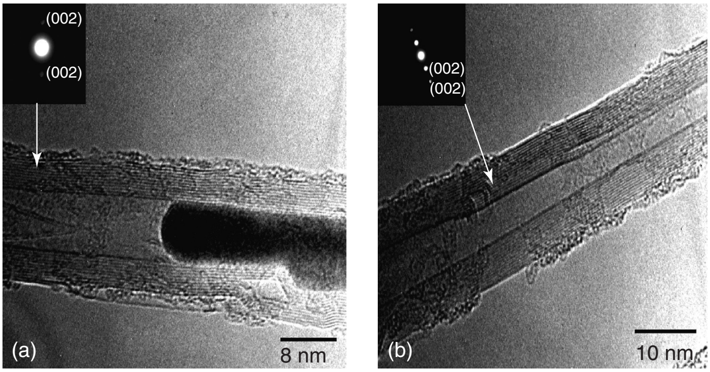

Figure 1.23 TEM images and selected-electron diffraction patterns of (a) CVD MWNT and (b) MWNT annealed at 2250 °C. (Source: Reproduced with permission from Ref. [81], Elsevier (2001).)

1.2.3 Characterization of Purified Carbon Nanotubes

The final quality and purity of purified CNTs can be examined by several analytical techniques including scanning electron microscopy (SEM), TEM, energy dispersive spectroscopy (EDS), Raman spectroscopy, AFM, X-ray diffraction

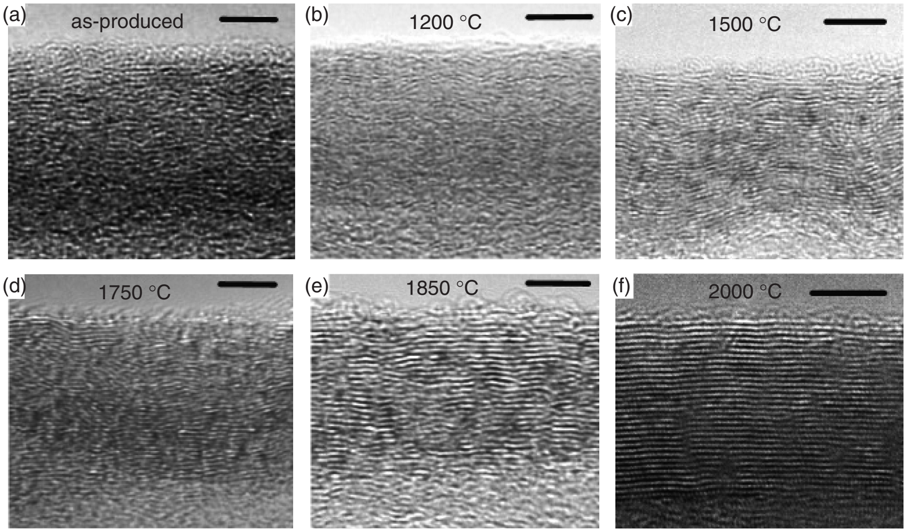

Figure 1.24 TEM images of the walls of (a) noncatalytic CVD-grown MWNTs in a porous alumina template and those annealed at (b) 1200 °C, (c) 1500 °C, (d) 1750 °C, (e) 1850 °C, and (f) 2000 °C. The initial, disordered carbon structure is converted into a more perfect graphitic structure with increasing annealing temperature. Scale bar is 5 nm. (Source: Reproduced with permission from Ref. [87], the American Chemical Society (2006).)

(XRD), ultraviolet-visible-near infrared (UV-vis-NIR), absorption spectroscopy, NIR spectroscopy, and thermogravimetric analysis (TGA). These have been recommended by the International Team in Nanosafety (TITNT) and NASA-Johnson Space Center (United States) as the characterization techniques for both the pristine and purified SWNTs [91, 92]. In general, SAED and TEM offer useful information relating the chemical identity of impurities of both the pristine and purified nanotubes. However, these techniques are unsuitable for quantitative evaluation of the purity of CNTs. Further, the sample preparation procedures for TEM examination are tedious and time consuming. The EDS attached to either SEM or TEM can provide characteristic X-ray peaks of various elements, particularly useful for qualitative assessment of the metallic impurities. The EDS/SEM is routinely used in the research institutions and industrial laboratories world wide for qualitative analysis of inorganic materials. The EDS/SEM can provide quantitative analysis if suitable standards are available. However, it is difficult to analyze and quantify light elements in the EDS spectra because of the absorption of their X-ray radiation by the window material (beryllium) of the spectrometer. This effect can be minimized by using an SEM-windowless EDS facility.

At present, there appears to be a need of reliable techniques for fast and accurate assessment of the nanotube purity. In this regard, Raman spectroscopy is particularly useful for qualitative analysis of purified nanotubes by examining vibrational frequency responses of different carbon species. The position, width and relative intensity of Raman peaks of various carbonaceous species (e.g., amorphous carbon, fullerene, diamond, and SWNT) are related to their sp^3 and sp^2 configurations [93–95]. Raman spectra of SWNTs are well characterized for the radial breathing mode (RBM) at 150–200 cm^{-1} and the tangential G-band at $\sim$1550–1605 cm^{-1} [94]. The tangential-mode G-band involves out-of-phase intralayer displacement in the graphene structure of the nanotubes. It is a measure of the presence of ordered carbon. Figure 1.25 shows the Raman profile of the SWNT. A band located at $\sim$1350 cm^{-1} is attributed to the disorder-induced band (D-band) and related to the presence of nanoparticles and amorphous carbon. Furthermore, a second-order mode at $\sim$2600 cm^{-1} is referred to the D^* mode, commonly known as the G' *mode*. The RBM is associated with the collective in-phase radial displacement of carbon atoms, and only can be found in the SWNTs. It gives direct information for the tube diameter since its frequency is inversely proportional to the tube diameter. The D-peak is absence in graphite and only found in the presence of disorder defects. The D- and G-peak ratio characterizes the disorder degree of the materials studied. Thus the purity level of SWNTs can be qualitatively determined from the D/G intensity ratio and the width of the D-band [95, 96]. The full width at half maximum (FWHM) of the D-band for the carbonaceous impurities is much broader than that of the SWNT. An asymmetry on the right-hand side of G-band is a peak characteristic of MWNTs and normally appears at 1620 cm^{-1} [97].

XRD is a nondestructive and useful material characterization technique for identifying the crystal structure, interlayer spacing, structural strain, and crystal orientation. It is a global characterization technique since all its data are averaged over the whole regions of the specimen. On the contrary, TEM-SAED can provide

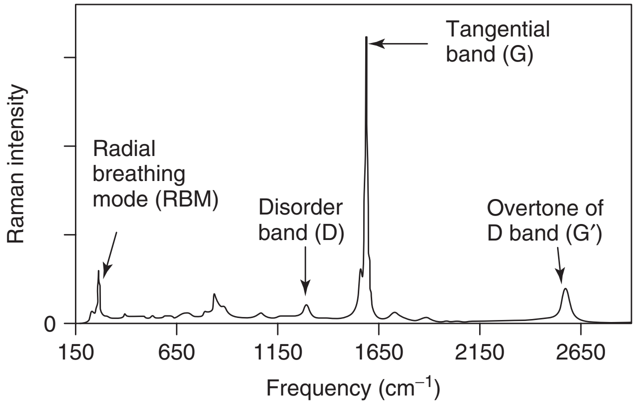

Figure 1.25 Raman profile of SWNT showing the presence of radial breathing mode and tangential G-band.

morphological and structural information at local levels. Thus a combination of these techniques can provide further insights into the structure and morphology of nanotubes after purification. Very recently, Vigolo *et al.* [98] used Raman, TEM, XRD, and infrared spectroscopy to assess the purity of arc-grown SWNTs containing Ni and Y catalyst nanoparticles (denoted as PS0). Three progressive purification steps were adopted: (i) air oxidation at 365 °C for 90 min (denoted as PS1), (ii) acid treatment in a 6N HCl solution for 24 h under reflux (denoted as PS2), and (iii) high-temperature annealing in vacuum (1100 and 1400 °C) for 1 h (denoted as PS3a and PS3b, respectively). Figure 1.26 shows Raman spectra of the specimens after each step of the purification procedures. The D-band range is given in the inset. The D-band becomes sharper after initial and second steps of purification and undergoes a slight upshift with a decrease in intensity. These result from the removal of carbonaceous impurities. The D-band intensifies after high-temperature annealing. Figure shows their corresponding XRD patterns. The reflections associated with the Ni nanoparticles can be readily seen in the pattern of pristine nanotube. A strong background at small wave vector $Q(=4\pi\sin\theta)/\lambda)$ below 1 Å^{-1} is apparent. This is associated with the (10) reflection of the SWNT bundles featuring as the nanoparticles in this background. A faint peak at ∼1.8 Å^{-1} reveals the presence of some graphitic particles. After air oxidation, NiO peaks derived from nickel oxidation are clearly visible. But weak reflections from nickel still remain. Most of the NiO Å^{-1} particles are removed after the HCl treatment. The (10) reflection and other (hk) reflections of the SWNT bundles are quite obvious at this stage. The intense peak at 1.8 Å^{-1} is assigned to the graphitic particles. The (hk) reflections from SWNT bundles become more intense after high-temperature annealing. The TEM images of the specimens after each step of the purification procedure are shown in Figure 1.28a–d. A large quantity of impurities including metal nanoparticles coated with amorphous carbon and graphitized carbon together with SWNT bundles can be seen (Figure 1.28a). The number of catalyst particles

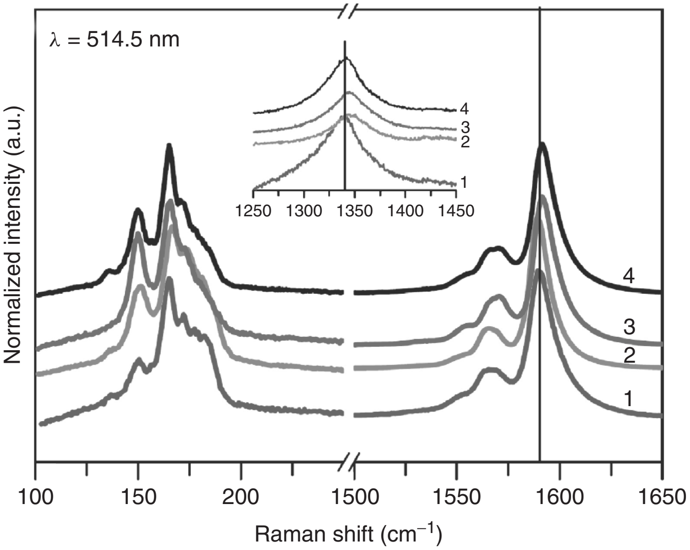

Figure 1.26 Raman spectra of arc-grown SWNT (PS0) after each step of the purification procedure. (1) PS0, (2) PS1, (3) PS2, and (4) PS3a. (Source: Reproduced with permission from Ref. [98], Elsevier (2010).)

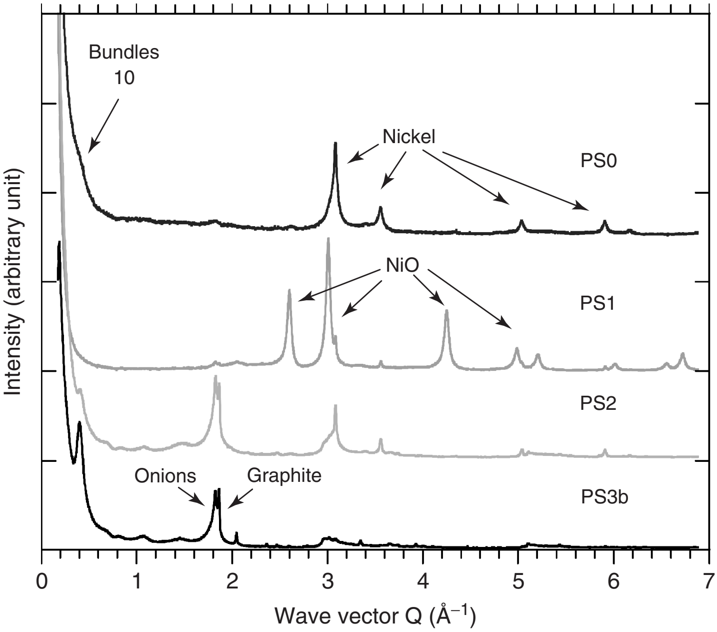

Figure 1.27 XRD patterns of PS0, PS1, PS2, and PS3b specimens. (Source: Reproduced with permission from Ref. [98], Elsevier (2010).)

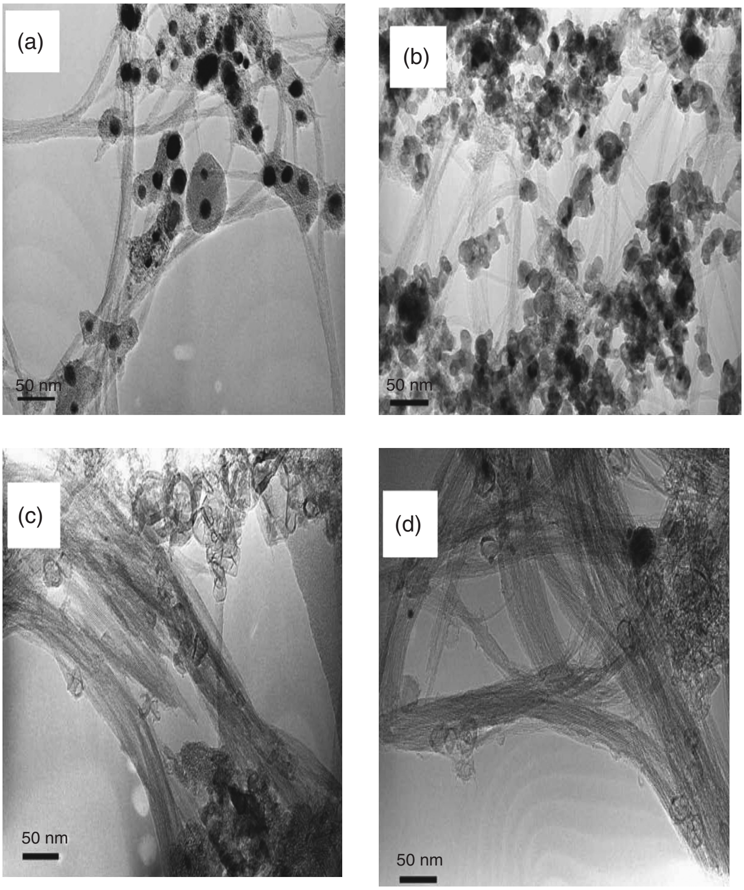

Figure 1.28 TEM images of (a) PS0, (b) PS1, (c) PS2, and (d) PS3a. (Source: Reproduced with permission from Ref. [98], Elsevier (2010).)

reduces significantly after acid treatment. Numerous empty carbon cells derived from the removal of catalyst particles are visible (Figure 1.28c).

TGA is a simple quantitative method for measuring the specimen mass in relation to changes in temperatures using a thermobalance. During the tests, the temperature is raised and the weight of the sample is recorded continuously, which permits the monitoring of weight losses with time. It can be performed in air, oxygen, or inert gas (or vacuum). TGA with air/oxygen atmosphere allows the determination of temperatures at which nanotubes and impurities oxidize. Since amorphous carbon, carbon nanoparticle, multishell carbon, fullerene and SWNT have different affinity toward oxygen, thus those impurities and CNTs oxidize at different temperatures as expected [99, 100]. Other quantitative method such as UV-vis-NIR spectroscopy has also been employed for purity evaluation of SWNTs [101, 102].

1.3
Carbon Nanofibers (CNFs)

Vapor-grown carbon nanofibers (VGCNFs) have received considerable attention in recent years because of their relatively low cost when compared to CNTs, especially SWNTs. Thus VGCNFs are an attractive alternative for CNTs for research purposes and technological applications. VGCNFs are also widely known as carbon nanofibers (CNFs). A CNF consists of stacked curved graphene layers forming cones or cups with an angle alpha with respect to the longitudinal axis of the fiber [103–107]. The stacked cone graphene sheets yield the so-called ''herringbone'' morphology, while the stacked-cup structure is referred to as a *bamboo feature*

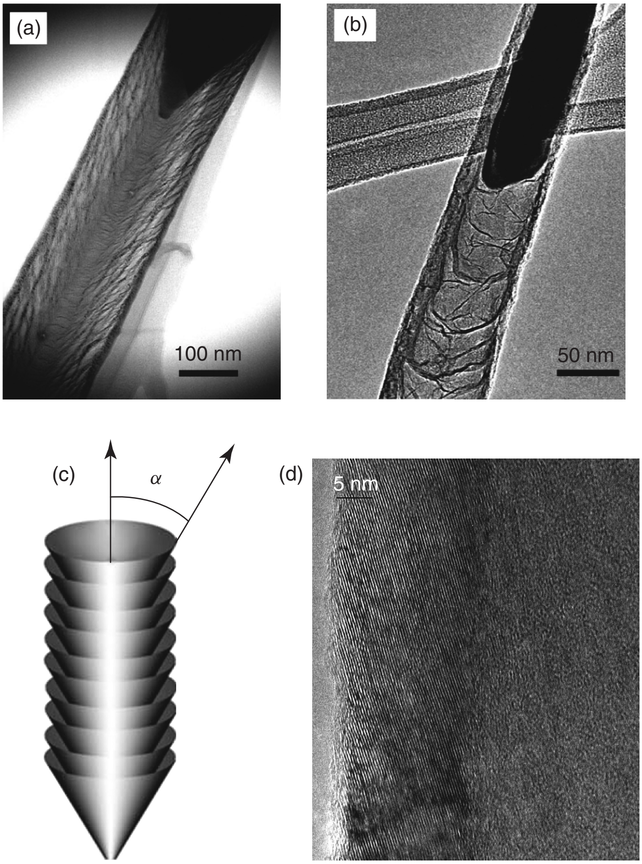

Figure 1.29 (a) STEM (scanning transmission electron microscopy) micrograph of a herringbone nanofiber and (b) TEM image of a bambootype CNF. (c) Schematic illustration of stacked cone (herringbone) nanofiber. (Source: Reproduced with permission from Ref. [103], American Institute of Physics (2005).) (d) TEM image of the VGCNF wall with canted graphene planes comprising of stacked-cup morphology. (Source: Reproduced with permission from Ref. [105], Elsevier (2007).)

(Figure 1.29a–d). The diameters of CNFs range from 50 to 500 nm. CNFs generally have more crystalline defects, rendering them exhibit poorer mechanical properties than MWNTs. Graphitization of MWNTs by high-temperature heat treatment can improve their electrical conductivity [87]. Analogously, graphitization can improve the perfection of grapheme planes in the walls of the VGCNFs. Tibbetts and coworkers [108] reported that heat treatment of CNFs at temperatures above 1500 °C results in significant rearrangement of the core morphology. Heat treatment at temperatures of 1800–3000 °C reduces the structural disorder and increases the graphitic content of the fiber [109, 110]. In other words, increasing graphitization temperature leads to a reduction of the turbostratic layer and an increase of the order in the graphene planes [106].

CNFs were produced commercially by the Applied Sciences, Inc. using high-temperature decomposition of natural gas in the presence of the $Fe(CO)_5$ catalyst (Figure 1.30). When the catalyst particles are properly dispersed and activated with sulfur, VGCNFs are abundantly produced in a reactor at 1100 °C [105]. This manufacturer has produced Pyrograf® III nanofibers of two types (PR-19 and PR-24) in four different grades, that is, as-grown (AS), pyrolytically stripped (PS), LHT and HHT [111]. Pyrograf®-III is available in diameters ranging from 70 to 200 nm and a length estimated to be 50–100 μm. The diameters of PR-19 and PR-24 fibers are about 150 and 100 nm, respectively. The AS fibers have polyaromatic hydrocarbons on their surfaces. The PS-grade fiber is pyrolytically stripped at 600 °C to remove polyaromatic hydrocarbons from the fiber surface. The LHT-grade nanofiber is treated at 1500 °C in order to carbonize and chemically vaporize deposited carbon present on the fiber surface, and the HHT-grade nanofiber is treated to temperatures up to 3000 °C, leading to graphitization of the fiber. On the other hand, vertically aligned CNFs designed for electronic device applications can be synthesized by means of PECVD process [103].

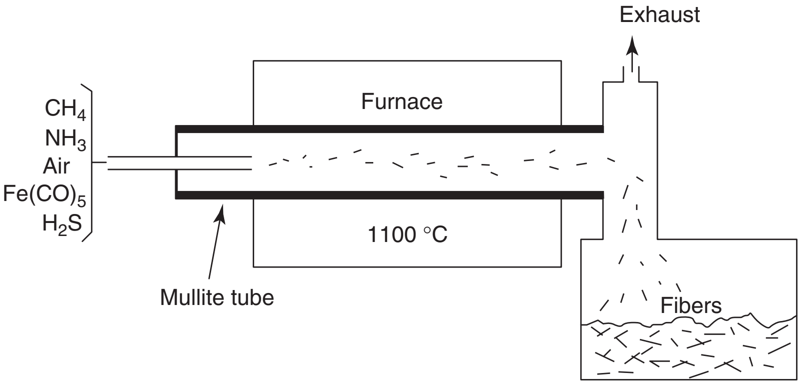

Figure 1.30 Apparatus for manufacturing VGCNFs. (Source: Reproduced with permission from Ref. [105], Elsevier (2007).)

1.4
Physical Properties of Graphene

1.4.1
Mechanical Behavior

The mechanical behavior of graphene can be determined from both theoretical modeling and experimental measurement. The numerical simulation methods commonly used for predicting mechanical behaviors of graphene are equivalent-continuum, quantum mechanical (QM) and atomistic modeling. Equivalent-continuum modeling is based on the well-established principles of elasticity of shells, beams, and rods. This method serves as a bridge between computational chemistry and solid mechanics by substituting discrete molecular structures with equivalent-continuum models [112]. For example, a beam undergoes stretching; bending and torsional deformation in structural mechanics can be used to mimic bond stretching, angle bending, and dihedral stretching of covalently bonded carbon atoms. Using this approach, Sakhaee-Pour [113] determined the elastic properties of a single-layered graphite sheet and reported that its Young-modulus (E) is around 1 TPa, regardless of the chirality. The QM calculations are performed using the density functional theory. The *ab initio* QM calculation for the phonon spectra of graphene as a function of uniaxial tension generates $E = 1.05$ TPa [114].

Atomistic simulation can reveal the physical nature of graphene mechanical deformation at atomistic scale using relevant interatomic potential energy models. In this regard, molecular dynamics (MD) is typically used to simulate the physical motion of atoms and molecules numerically. The atoms are allowed to interact for a period of time, giving rise to the movement and force field among them. The trajectories of atoms in the system under consideration can be estimated from the Newtonian equation of motion. The potential energy of the system is a function of the positions of atoms and thus can be described in terms of force field functions and parameters. Several interatomic potentials have been developed for use with a select group of materials including Lennard-Jones, Morse and Tersoff-Brenner potentials [115]. Lennard-Jones and Morse potentials introduced in the 1920s are empirical isotopic pair potentials and particularly suitable for atoms with no valence electrons. The Tersoff-Brenner potential is widely used for simulations in the carbon-based materials such as diamond, graphene, and nanotubes.

The mechanical deformation of graphene can be predicted by MD simulations using appropriate interatomic potential models under tensile/shear loadings. Thus the Young's modulus and shear modulus of graphene can be determined accordingly. In general, there exists two kinds of atomistic interactions between the carbon atoms, that is, covalently bonded and nonbonded. The potential energy of graphene is derived from covalently bonded atom interactions such as bond stretching, bond angle bonding, dihedral angle torsion and inversion, as well as nonbonded interaction (van der Waals force) characterized by Lennard-Jones potential [116]. Tsai and Tu employed MD simulations for predicting mechanical properties of a single graphite layer using these assumptions and obtained a stiffness value of 0.912 TPa. Jiang *et al.* [117] used MD to obtain thermal vibrations of graphite and then evaluate the Young's modulus from the thermal mean-square vibration amplitudes. They indicated that the Young's modulus increases from 0.95 to 1.1 TPa as the temperature increases from 100 to 500 K. In recent years, coupled quantum mechanical/molecular mechanical (QM/MM) calculations have been for mechanical modeling for the graphene sheet [118, 119]. Kim and coworkers [119] determined $E = 1.086$ TPa for armchair graphene and $E = 1.05$ TPa for zigzag graphene using the QM/MM simulations.

The experimental measurements of mechanical properties of pure graphene are known to be difficult and tedious. Lee *et al.* [120] obtained a Young's modulus of 1.02 TPa and intrinsic tensile strength (σ) of 130 GPa for a defect-free graphene monolayer via nanoindentation using an AFM. Using a similar method, the E values of graphene bilayer and trilayer were determined to be 1.04 and 0.98 TPa, while the σ values to be 126 and 101 GPa, respectively [121]. Gomez-Navarro *et al.* [122] obtained $E = 0.25$ TPa for freely suspended rGO monolayer, being a quarter of that of pristine graphene. The Young's modulus was determined through a tip-induced deformation by indenting an AFM tip at the center of the suspended layer.

The graphene paper produced by dispersing GO sheets in water followed by filtration and air drying, displaying $E = 25.6$ GPa and σ of 81.9 MPa. These GO colloids modified with either MCl_2 salts (M = Mg or Ca) followed by filtration and air drying, showing Young's modulus in the range of 24.6–28.2 GPa and ultimate tensile stress in the range of 87.9–125.8 MPa [123]. The Mg^{2+} or Ca^{2+} ions can bind oxygen functional groups on the basal planes and the carboxylate groups on the edges of the GO sheets, thereby improving their mechanical properties. Table 1.2 summarizes experimental tensile properties of graphene and chemically rGO specimens. Commercial exfoliated GNP comprising multiple stacked graphene sheets with a trade name of "xGnP" (XG Sciences) is reported to have tensile modulus and strength of ~1 TPa and ~10–20 GPa, respectively [124].

1.4.2
Electrical Behavior

Graphene exhibits excellent electron mobility in excess of 200 000 $cm^2\ V^{-1}\ s^{-1}$ [125, 126]. GO is electrically insulating; hence, additional chemical reduction and thermal annealing treatments are needed for eliminating oxygen functional groups. These treatments partially restore its electrical conductivity. The conductivity of rGO generally ranges from 0.05 to 500 $S\ cm^{-1}$ depending on the degree of deoxygenation. The residual oxygen forms sp^3 bonds with carbon atoms in the basal plane of rGO. The sp^3 bonds disrupt charge transport in the sp^2 carbon clusters, thereby reducing electrical conductivity of rGO. Mattevi *et al.* studied the effect of sp^2 carbon fractions on the conductivity of GO treated by chemical reduction and thermal annealing [29]. The conductivity can be tailored over about 12 orders of magnitude by increasing sp^2 graphene domain fractions (Figure 1.31). At

Table 1.2 Tensile properties of graphene and its derivatives.

Research group	Material	Facility	Young's modulus (GPa)	Tensile strength (GPa)	Year
Lee *et al.* [120]	Graphene monolayer	AFM	1.02×10^3	130	2008
Lee *et al.* [121]	Graphene bilayer	AFM	1.04×10^3	126	2009
Lee *et al.* [121]	Graphene trilayer	AFM	0.98×10^3	101	2009
Gomez-Navarro *et al.* [122]	rGO monolayer	AFM	250	–	2008
Park *et al.* [123]	GO paper	DMA at 35 °C	25.6	81.9×10^{-3}	2008
Park *et al.* [123]	Mg-modified GO paper	DMA at 35 °C	24.6	87.9×10^{-3}	2008
Park *et al.* [123]	Rinsed Mg-modified GO paper	DMA at 35 °C	27.9	80.6×10^{-3}	2008
Park *et al.* [123]	Ca-modified GO paper	DMA at 35 °C	21.5	75.4×10^{-3}	2008
Park *et al.* [123]	Rinsed Ca-modified GO paper	DMA at 35 °C	28.1	125.8×10^{-3}	2008

DMA, dynamic mechanical analyzer.

low sp^2 fractions, rGO contains a large number of oxidized domains; thus hopping or tunneling transport among the sp^2 clusters is expected. By increasing the sp^2 fraction to more than 0.9, the conductivity of rGO or TRG sheets approaches that of graphene.

Chen *et al.* [127] fabricated freestanding graphene paper by vacuum filtration of rGO suspensions through a commercial membrane filter, followed by air drying and peeling from the filter membrane. The as-produced paper had electrical conductivity of about $30\,\mathrm{S\,cm^{-1}}$ but increased to 118 and $351\,\mathrm{S\,cm^{-1}}$ by heat treating at 220 and 500 °C, respectively. Ruoff and coworkers [128] reported that the electrical conductivity of freestanding rGO paper is $6.87 \times 10^2\,\mathrm{S\,m^{-1}}$. Very recently, Schwamb *et al.* [129] indicated that the electrical conductivity of TEGO flake is in the range of 6.2×10^2 to $6.2 \times 10^3\,\mathrm{S\,m^{-1}}$.

1.4.3
Thermal Behavior

Recently, Baladin and coworkers [130, 131] achieved very high thermal conductivity (κ) of $4840–5300\,\mathrm{Wm^{-1}K^{-1}}$ for a single-layer graphene (SLG) produced by mechanical cleavage of bulk graphite. During the measurements, a single graphene layer suspended a trench in Si/SiO_2 substrate was irradiated with a laser beam of 488 nm wavelength. The heat was transferred laterally toward the sinks made

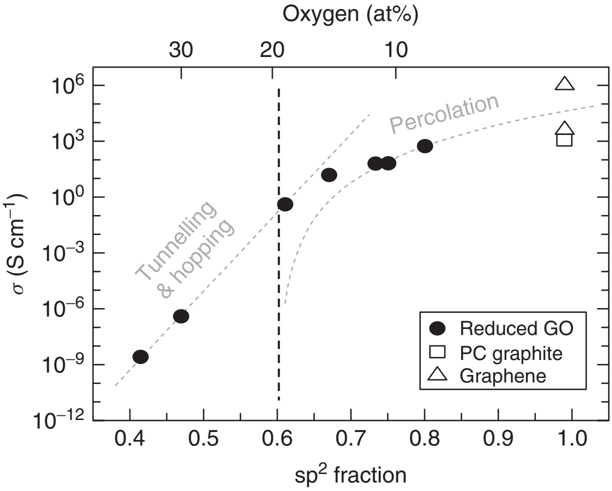

Figure 1.31 Conductivity of thermally reduced GO versus sp^2 carbon fraction. The vertical dashed line indicates the percolation threshold at sp^2 fraction of ~0.6. Fitting of the experimental data reveals two different regimes for electrical transport with sp^2 fraction. Tunneling and/or hopping (straight dashed line) mechanisms dominate at sp^2 fractions below 0.6, while percolation amongst the sp^2 clusters dominates above the percolation threshold. The 100% sp^2 materials are polycrystalline (PC) graphite and graphene. (Source: Reproduced with permission from Ref. [29], Wiley-VCH (2009).)

from graphitic layers (Figure 1.32). The amount of power dissipated in graphene and corresponding temperature rise were determined from the spectral position and integrated intensity in the graphene G-peak using confocal micro-Raman spectroscopy. SLG is commonly supported on a dielectric substrate for electronic device applications. Thus fully contact with a substrate could affect the thermal transport property of graphene. Ruoff and coworkers [132] made thermal measurements on an SLG supported on amorphous SiO_2 substrate, reporting a κ value of 600 W m^{-1} K^{-1} near room temperature. The fall in the κ value of graphene supported on SiO_2 is due to the scattering by substrate phonons and impurities. Schwamb *et al.* [129] determined the κ value of thermally reduced GO flake to be 0.14–2.87 W m^{-1} K^{-1}. Very recently, Xiang and Drzal [20] fabricated freestanding GNP paper by vacuum filtration of GNP suspension using an ANODISC membrane (0.2 μm, Whatman) (Figure 1.33). After filtration, the paper was suction dried and placed in a vacuum oven at 60 °C overnight before peeling the GNP paper off the membrane. The ''as-made'' freestanding paper was annealed at a furnace at 340 °C for 2 h and termed as *annealed* paper. The annealed paper was finally cold pressed at 100 psi at room temperature for 1 h and identified as 'annealed and cold pressed' (Figure 1.34a,b). The paper has the advantages of ease of handling and storage in readiness for its incorporation into polymers to form strong and conducting nanocomposites for industrial applications. The in-plane thermal conductivities of

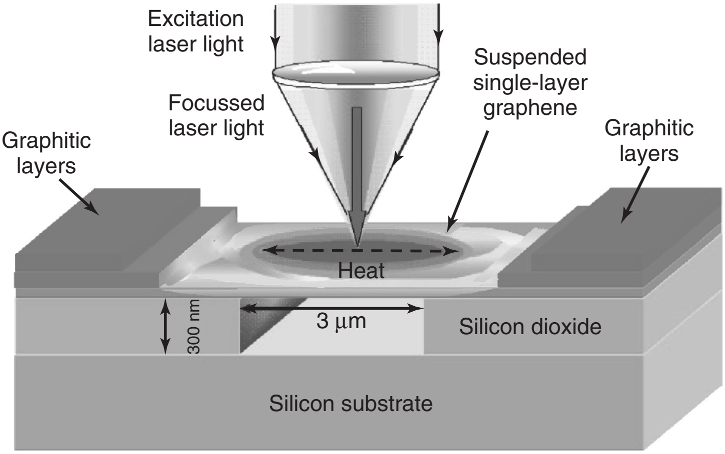

Figure 1.32 Schematic diagram showing the excitation laser beam focused on a graphene layer suspended across a trench. Laser beam creates a local hot spot and generates a heat wave inside SLG propagating toward heat sinks. (Source: Reproduced with permission from Ref. [130], the American Chemical Society (2008).)

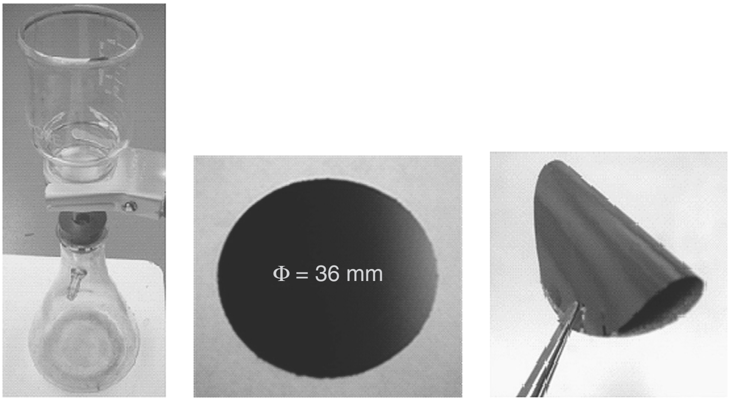

Figure 1.33 Photographs of the filtration device, a sample of GNP paper peeled off the ANODISC filter paper and a mechanical flexible GNP paper. (Source: Reproduced with permission from Ref. [20], Elsevier (2011).)

the as-prepared, annealed (340 °C for 2 h), and annealed and cold-pressed GNP papers are 98, 107, and 178 $\mathrm{W\,m^{-1}\,K^{-1}}$, respectively. Cold pressing improves the thermal contact by eliminating most of the pores in the paper, resulting in highest thermal conductivity. The through-plane thermal conductivities of the as-prepared, annealed (340 °C for 2 h), and annealed and cold-pressed GNP papers are 1.43, 1.71, and 1.28 $\mathrm{W\,m^{-1}\,K^{-1}}$, respectively.

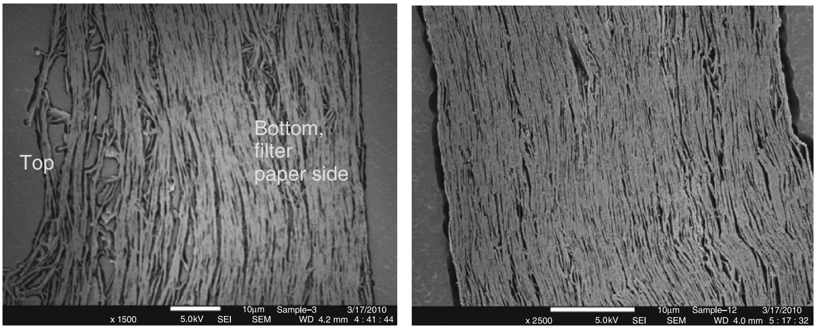

(a) (b)

Figure 1.34 Scanning electron micrographs of cross section of the (a) as-made GNP paper and (b) annealed and cold-pressed GNP paper. (Source: Reproduced with permission from Ref. [20], Elsevier (2011).)

1.5
Properties of Carbon Nanotubes

1.5.1
Mechanical Behavior

1.5.1.1 Theoretical Prediction

Basic understanding of the mechanical properties of CNTs, such as the Young's modulus, strength and fracture strain, is essential for the development of their technological applications. The Young's modulus of a material is generally related to the chemical bonding of its constituent atoms. The interaction forces between atoms are typically represented in the form of interatomic potential energy models. Many theoretical and experimental investigations have been carried out to determine the Young's modulus of CNTs. Theoretical studies show that the Young's modulus varies greatly from 0.6 to 5.5 TPa [133–138]. A large variation in predicted mechanical stiffness arises from the different methods used for the simulations, different CNT chiralities or lengths, different potentials used to define the C–C bond in the plane of the graphene sheets, and the presence of intrinsic defects.

Yakobson *et al.* [133] employed MD simulations to determine the Young's modulus of SWNTs under axial compression. The Tersoff-Brenner potential was used for characterizing the C–C interactions. They obtained a Young's modulus of 5.5 TPa. The simulation also predicts that SWNTs can sustain a large strain of 40% without damaging its graphitic structure. Robertson *et al.* [134] adopted empirical Brenner potential to examine the energetics and elastic properties of CNTs with radii <9 Å. The Young's modulus of CNTs was close to that of in-plane graphene, that is, ~1.06 TPa. Yao and Lordi [135] employed MD simulations with the universal force field and reported a stiffness value of ~1 TPa for SWNTs. Furthermore, the Young's modulus was found to increase significantly with decreasing tube diameter and increase slightly with decreasing tube helicity. Hernandez *et al.* [136] employed a tight-binding model to calculate the Young's modulus of SWNTs. The stiffness was dependant on the diameter and chirality of the CNTs, ranging from 1.22 TPa for the (10,0) and (6,6) tubes to 1.26 TPa for the (20,0) tube. Haskins *et al.* [137] also used a tight-binding MDs to predict the Young's modulus of nanotubes. For a pristine (5,5) nanotube, the stiffness was calculated to be ∼1.1 TPa. Very recently, Qin *et al.* used Lennard-Jones potential for the MD simulations. The predicted modulus of the (5,5) and (9,0) SWNTs ranges from 0.6 to 0.7 TPa [138]. Apparently, most MD simulations produce a stiffness value of around 1 TPa. The predicted Young's modulus of around 1 TPa is acceptable for the SWNT since it is close to that of the graphene sheet.

1.5.1.2 **Experimental Measurement**

Experimental measurements of the Young's modulus of CNTs are mostly conducted in electron microscopes and AFMs [139–144]. Treacy *et al.* [139] determined the Young's modulus of individual MWNTs (arc-grown) anchored in a TEM from their amplitudes of thermal vibrations. They obtained an average value of 1.8 TPa with a large scatter in the data ranging from 0.4 to 4.15 TPa. A similar method was adopted by Krishnan *et al.* [140] for measuring the stiffness of MWNTs synthesized by the laser ablation process, producing a value of 1.25 TPa. Considering CNT acts as a cantilever beam under bending in an AFM. The cantilever deflection and force applied can be measured accordingly. Using this technique, Wong *et al.* [141] obtained a stiffness value of 1.28 TPa for arc-grown MWNTs. Salvetat *et al.* [142] obtained the Young's modulus values of both the arc- and CVD-grown MWNTs to be 0.81 and 0.027 TPa, respectively. Arc-grown MWNTs exhibit higher Young's modulus because of their more perfect crystalline structure. Yu *et al.* [143] used a tensile testing tool inside an SEM to study the tensile behavior of MWNTs. An *in situ* AFM tip was employed to assist the manipulation, attachment, and stretching of MWNTs. They reported the Young's modulus values ranging from 0.29 to 0.95 TPa and a strain at break of up to 12%. The failure of the MWNT under tensile load can be described in term of the "sword-in sheath" type mode, in which the outermost shell fails first followed by the sliding and pulling out of internal shells from the outer shell of the MWNT [144]. Yu *et al.* [145] then used a similar method for tensile loading of SWNT ropes and reported Young's modulus values of 0.32–47 TPa with a mean value of 1 TPa. Demczyk *et al.* [146] *in situ* tensile loaded arc-grown MWNT in a TEM, obtaining a Young's modulus of 0.9 TPa and a tensile strength of 150 GPa.

Raman spectroscopy has been used to extract the mechanical properties of CNTs embedded in a polymer resin [147, 148]. For example, Lourie and Wagner [147] employed micro-Raman spectroscopy to monitor cooling-induced compressive deformation of CNTs embedded in an epoxy matrix. The thermal stress induced can cause a shift in the G′-band. Cooper *et al.* [148] used a self-made four-point bending rig and placed on the Raman microscope stage to induce mechanical deformation for the CNT/epoxy specimens. From the shift in the G′-band as a result of tensile deformation on the specimen surfaces, the effective moduli of arc-/laser-grown SWNTs and arc-grown MWNTs dispersed in the composites are ∼1 and 0.3 TPa, respectively. Table 1.3 summarizes experimental values of

Table 1.3 Experimental young's modulus and tensile strength of CNTs determined using electron microscopic and raman spectroscopic facilities.

Research group	Nanotube type	Young's modulus (TPa)	Tensile strength (GPa)	Year
Treacy *et al.* [139]	MWNT	1.8	–	1996
Wong *et al.* [141]	MWNT	1.28	–	1997
Krishnan *et al.* [140]	SWNT	1.25	–	1998
Salvetat *et al.* [142]	MWNT	0.81	–	1999
Salvetat *et al.* [142]	MWNT	0.027	–	1999
Yu *et al.* [143]	MWNT	0.27–0.95	11–63	2000
Yu *et al.* [145]	SWNT rope	0.32–1.47	13–52	2000
Cooper *et al.* [148]	SWNT	1	–	2001
Cooper *et al.* [148]		0.3	–	2001
Demczyk *et al.* [146]		0.9	150	2002

MWNTs and SWNTs determined from different techniques. A large variation in experimental values of Young's modulus of CNTs is observed. This is attributed to the difficulty in manipulating and measuring individual nanotubes of nanometer dimension [149]. Furthermore, the CNTs listed in this table were synthesized from either PVD or CVD techniques, having different nanotube types, impurity contents, lengths, and diameters.

1.5.1.3 Flexibility of Carbon Nanotubes

Iijima *et al.* [150] employed the Tersoff-Brenner potential for simulating the bending behavior of SWNTs of different diameters and helicity. Their results showed that the nanotubes are extremely flexible on the application of large deformation strains. The hexagonal network of CNTs is resilient and can resist bond breaking up to a very high strain values. The network can be preserved even by bending up to $\sim 110^\circ$, forming a kink consequently. The kink enables the nanotubes to relax elastically. Furthermore, HRTEM observation also provides a substantial evidence for the formation of a single kink or multiple kinks in the CNTs on bending (Figure 1.35a–d). Falvo *et al.* [151] employed AFM to observe bending features of MWNTs up to a 42% strain value. They found that the nanotubes exhibit very high flexibility and possess the ability to buckle elastically through large angles without inducing visible defects. This is an interesting and important feature of CNTs, demonstrating their good ductile characteristics. The fracture tensile strain predicted by MD simulations could reach up to 30% [152], or even higher depending on simulated temperatures and interatomic potentials employed [153]. The tensile fracture strain of SWNTs at room temperature is 15% or higher and could reach up to 280% at temperatures $\geq 2000\,^\circ\mathrm{C}$ [154].

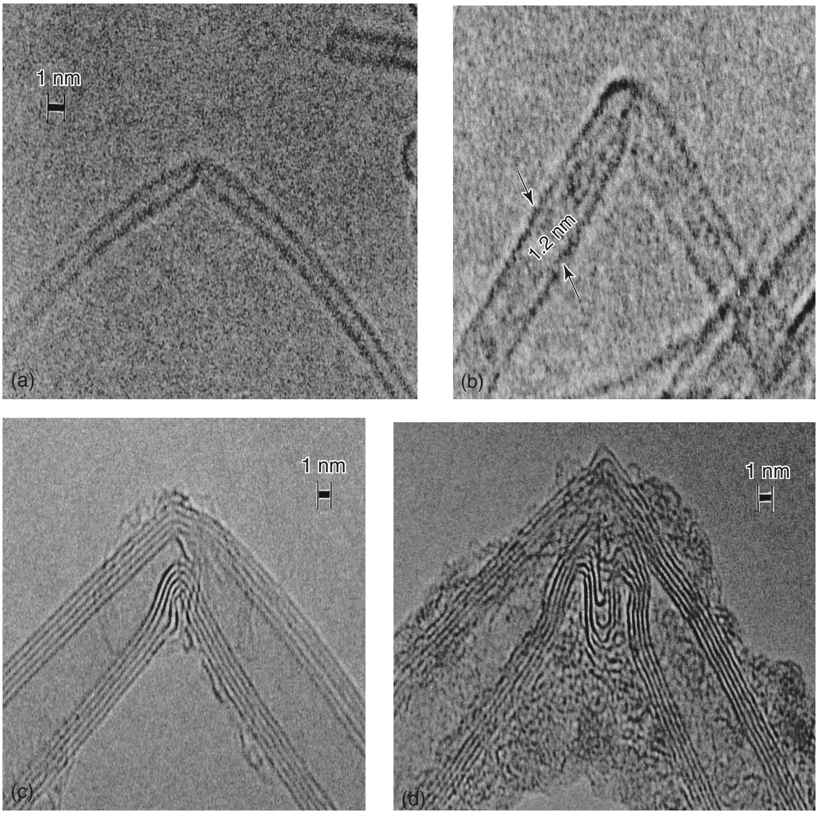

Figure 1.35 HRTEM images of kink structures formed in SWNTs and MWNTs under mechanical bending. A single kink in the middle of SWNTs with diameters of (a) 0.8 and (b) 1.2 nm. MWNTs with (c) single-kink and (d) two-kink complex. (Source: Reproduced with permission from Ref. [150], The American Institute of Physics (1996).)

1.5.2
Electrical Behavior

The sp^2 carbon bonding in the CNTs gives their π electrons very large mobility. The electrical conductivity of CNTs varies from metallic to semiconducting depending on their chirality and diameter. Armchair SWNTs ($n = m$) possess a large carrier concentration, rendering them metallic in nature. In contrast, zigzag and other chiral nanotubes exhibit semiconducting to semimetallic behavior since they possess medium to small band gaps between the valence and conduction bands. The electrical conductivity of SWNT ropes is reported in the range of 1×10^4 to $3 \times 10^4\ \mathrm{S\,cm^{-1}}$ at 300 K [155, 156]. The agglomeration of nanotubes into ropes may degrade the conductivity of SWNTs. The individual tubes of an MWNT may have different chiralities. Accordingly, a single MWNT may have both metallic and semiconducting layers. The electrical conductivity of carbon arc-grown MWNTs determined from the four-point technique ranging from ~1.25 to 2×10^5 S cm^{-1}, corresponding to semiconducting to metallic behavior [157]. High-temperature annealing can enhance electrical conductivity of CNTs synthesized by CVD. The conductivity of MWNTs produced by noncatalytic CVD in a porous alumina template increases from about 1×10^4 to 2×10^5 S m^{-1} after annealing at 2000 °C. This is due to the perfection in the structure of nanotubes walls by high-temperature annealing [87].

Electrons in one-dimensional CNTs are believed to conduct ballistically. In this regard, electrons experience no resistance in the CNTs. An ideal metallic SWNT is predicted to have a quantum conductance (Go) of 2 Go defined by the following equation [158]

$$\mathrm{Go} = \frac{2e^2}{h} = (12.9\,\mathrm{k\Omega})^{-1} \tag{1.5}$$

where e is electronic charge and h the Plank's constant. Frank *et al.* determined the electrical conductance of MWNT using a scanning probe microscope attached with a nanotube fiber. They found that the nanotube conducts current ballistically with quantized conductance behavior. The MWNT conductance jumped by the increments of one unit of Go [159].

1.5.3
Thermal Behavior

The transport of thermal energy in CNTs is known to occur via phonon conduction mode. The phonon thermal conductivity can be determined from $\kappa = C_\mathrm{p} v \lambda$ where C_p is the specific heat, v the speed of sound and λ the mean free path of phonon. The mean free path is the average distance travels by a phonon between successive scatterings and estimated to be greater than 1 μm [160]. Thus thermal conductivity of CNTs depends mainly on the mean free path of phonons and temperature [161]. When SWNTs have comparable or shorter length than the free path of phonons, they can be considered as ballistic phonon conductors at low temperatures with four quanta of thermal conductance (Goth) given by Schwab *et al.* [162]

$$\mathrm{Go}^{\mathrm{th}} = \pi^2 k_\mathrm{B}^2 T/3h \tag{1.6}$$

where k_B is a Boltzmann constant. The factor of T in thermal quantum conductance implies its linear dependance on temperature. In the case of electronic conduction, the corresponding quantity is the electron charge, e, and the electrical quantum conductance given by Eq. (1.5) is temperature independent. The ballistic thermal conductivity of CNTs increases linearly with temperature at low-temperature regime (~1–50 K) [161]. As the temperature increases, both acoustic and optical phonons involve in the transport, hence reducing the phonon mean free path. At higher temperatures, inelastic Umklapp scattering becomes dominant. It is noted that the thermal conductivity of nanotubes is also affected by the structural defects and impurities induced in the tubes during synthesis.

Theoretical MD simulation prediction exhibits an unusually high value of thermal conductivity, that is, 6600 W m^{-1} K^{-1} at room temperature for the (10,10)

Table 1.4 Room temperature thermal conductivity of carbonaceous materials.

Research group/ company	Material	Thermal conductivity ($W\,m^{-1}\,K^{-1}$)	Method	Specimen testing condition
Baladin *et al.* [130]	SLG	~4840–5300	Optical	Individual, suspended
Seol *et al.* [132]	SLG	600	Electrical	Supported on a substrate
Schwamb *et al.* [129]	TEGO	0.14–2.87	Electrical	Individual, suspended
Pop *et al.* [167]	SWNT	~3500	Electrical	Individual, suspended
Hone *et al.* [164]	SWNT	1750–5800	Thermocouples	Bundles
Kim *et al.* [165]	MWNT	>3000	Electrical	Individual, suspended
Fuji *et al.* [166]	MWNT	2069	Electrical	Individual, suspended

SWNT [160]. Osman and Srivastava determined thermal conductivity of SWNTs at 100–500 K using MD simulations with the Tersoff-Brenner potential for C–C interactions [163]. The temperature dependance of the thermal conductivity of nanotubes exhibits a peak behavior before falling off at higher temperatures. This is due to the onset of anharmonic Umklapp phonon scattering. The armchair (5,5) SWNT displays a κ value of ~2250 $W\,m^{-1}\,K^{-1}$ at room temperature (Table 1.4).

Pop *et al.* [167] determined the thermal properties of a suspended SWNT of length 2.6 μm and diameter 1.7 nm at 300–800 K by means of electrical measurements. The κ value is about 3500 $W\,m^{-1}\,K^{-1}$ at room temperature. Hone *et al.* [164] determined thermal conductivity of SWNT ropes using typical thermocouple measurements, obtaining κ value of 1750–5800 $W\,m^{-1}\,K^{-1}$ at room temperature. Fuji *et al.* [166] used a suspended sample-attached *T*-type nanosensor and reported that the thermal conductivity of a single MWNT at room temperature increases with decreasing tube diameter. The conductivity of an MWNT with an outer diameter of 9.8 nm is 2069 $W\,m^{-1}\,K^{-1}$ and decreases to about 500 $W\,m^{-1}\,K^{-1}$ for a tube of 28.2 nm. Kim *et al.* [165] ed a suspended microdevice and found that the thermal conductivity of an MWNT is more than 3000 $W\,m^{-1}\,K^{-1}$ at room temperature. Yi *et al.* [168] stripped CVD-grown MWNT bundles from their aligned arrays and obtained κ value of 25 $W\,m^{-1}\,K^{-1}$ using a self-heating 3ω method. The large difference between the thermal conductivity of a single tube and MWNT bundles can be attributed to high thermal contact resistance (Kapitza resistance), intertube Umklapp scattering and the presence of defects [168, 169].

1.6
Properties of Carbon Nanofibers

VGCNFs have larger diameters but lower crystallinity than the MWNTs. The mechanical properties of VGCNFs are generally poorer than the MWNTs. The tensile properties of VGCNFs depend greatly on the graphitization heat treatment. Very recently, Ozkan *et al*. [170] reported that the Young's modulus and tensile strength of Pyrograf® III PR-24 nanofiber of PS grade are 180 GPa and tensile strength of 2.9 GPa, while those of the HHT-grade are 245 and 2.35 GPa, respectively. Thus graphitization treatment increased the nanofiber elastic modulus by 35% because of the reduction of the outermost turbostratic layer and the increase of the order in the graphene planes. The thermal conductivity of VGCNF is reported to be 1950 W m^{-1} K^{-1} by the manufacturer [111].

1.7
Current Availability of Carbonaceous Nanomaterials

The demands for carbonaceous nanomaterials are ever increasing today because of their attractive applications in biomedical and technological sectors. Extensive research studies have been carried out in worldwide research institutions and industrial laboratories on the issues relating to the improvement of the synthesis techniques and physical/mechanical properties of carbon nanostuctures. Several patents have been granted recently by the US Patent and Trademark Office, and European Patent office for innovative synthesis processes of carbon nanomaterials (Tables 1.5 and 1.6). These offices granted exclusive rights for the researchers for their novel synthesis of carbonaceous materials. These patents form the basis for successful commercialization of carbonaceous nanomaterials. Further, global industrial manufacturers also produce carbon nanostructures of high qualities to meet the demands of academic research and technological application. The current availability of some carbonaceous nanomaterials is listed in Table 1.7.

1.8
Multifunctional Composite Materials

Conventional polymer composites have been extensively used as structural materials for industrial applications because of their light weight, high mechanical strength and excellent corrosion resistance. A typical example is carbon fiber/epoxy composites showing high-end applications in the aerospace and military sectors. They have successfully replaced most metallic components for structural engineering applications. However, the limits of improving properties of microcomposites have been reached because the need of using high filler volume contents for achieving required physical and mechanical properties. Large-volume fractions of fillers with micrometer dimensions have adverse effects on the processing and mechanical properties of resulting polymer composites.

Recent advances in nanotechnology have provided great opportunities for developing advanced techniques to synthesize novel nanomaterials with functional properties. These include nanoceramics (e.g., clay platelets, alumina, silica, silicon carbide, titania, zinc oxide, etc.) and carbonaceous nanomaterials. Nanomaterials can be added in very low loading levels to polymers for enhancing their properties. The physical and mechanical properties of polymer nanocomposites

Table 1.5 Patent processes for manufacturing graphenelike sheets and graphite nanoplatelets.

Patent number and year	Patent title	Inventor	Assignee
US 7658901 (9 February 2010)	Thermally exfoliated graphite oxide	Prud'Homme, R.K., Aksay, I.A., Adamson, D., Abdala, A.	Princeton University (USA)
US 7771824 (10 August 2010)	Bridged graphite oxide materials	Herrera-Alonso, M., McAllister, M. J., Aksay, I.A., Prud'Homme, R.K.	Princeton University (USA)
US 7785557 (31 August 2010)	Method of producing a graphene film as transparent and electrically conducting material	Gruner, G., Hecht, D., Hu, L.B.	Unidym, Inc. (USA)
US 7550529 (23 June 2009)	Expanded graphite and products produced therefrom	Drzal, L.T., Fukushima, H.	Michigan State University (USA)
US 7785492 (31 August 2010)	Mass production of nano-scaled platelets and products	Jang, B.Z., Zhamu, A., Guo, J. S.	Nanotech Instruments, Inc. (USA)
US 7799309 (21 September 2010)	Area weight uniformity flexible graphite sheet material	Reynolds III, R.A., Greinke, R.A.	Graftech International Holdings, Inc. (USA)
US 7824651 (2 November 2010)	Method of producing exfoliated graphite, flexible graphite and nano-scaled graphene platelets	Zhamu, A., Shi, J.J., Guo, J. S., Jang, B. Z.	Nanotech Instruments, Inc. (USA)

differ substantially from those of traditional composite counterparts. For example, clay silicates have been incorporated into polymers to improve their mechanical strength, flame retardancy and gas barrier resistance because of their abundancy and low cost [171, 172]. To achieve these desired properties, clay silicate must delaminate into individual nanoplatelets in the polymer matrix to produce exfoliated clay/polymer composites. However, hydrophilic clay silicates show poor dispersion in the polymer matrix because of their high tendency to agglomerate into large clusters. To increase their compatibility with the polymers, clay silicate surfaces are commonly modified with organic surfactants such as $R - NH_3^+$, yielding the so-called organoclays. The use of organomodifiers increases the production cost of polymer nanocomposites. Alkylammonium surfactants generally exhibit low thermal stability since they decompose into organic constituents during melt processing at high temperatures [173]. This case becomes even more serious for

Table 1.6 Patent processes for producing carbon nanotubes.

Patent number and year	Patent title	Inventor	Assignee
US 6413487 (2 July 2002)	Method and apparatus for producing carbon nanotubes	Resasco, D.E, Kitiyanan, B., Alvarez, W.E. Balzano, L.	University of Oklahoma (USA)
US 6962892 (8 Nov 2005)	Metallic catalytic particle for producing single-walled carbon nanotubes	Resasco, D.E, Kitiyanan, B., Harwell, J.H., Alvarez, W.E	University of Oklahoma (USA)
EP 1401763 B1 (30 Mar 2005)	Catalyst supports and carbon nanotubes produced thereon	Nagy, J., Nagaraju, N., Willems, I., Fonseca, A.	Facultes Universitaires Notre-Dame de la Paix (Belgium)
EP 1413551 B1 (21 July 2010)	Methods of manufacturing multiwalled carbon nanotubes	Sakurabayashi, Y., Kondo, T., Yamazawa, Y., Suzuki, Y., Monthioux, M. LeLay, M.	Toyota Jidosha Kabushiki Kaisha (Japan)
EP 1968889 B1 (10 Aug 2011)	Method for synthesis of carbon nanotubes	Bordere, S., Gaillard, P., Baddour, C.	Arkema France (France)
US 7993620 (9 Aug 2011)	Systems and methods for the formation and harvesting of nanofibrous materials	Lashmore, D.S., Brown, J.J., Chaffee, J.K., Resnicoff, B. Antoinette, P.	Nanocomp Technologies, Inc. (USA)
US 8057777 (15 Nov 2011)	Systems and methods for controlling chirality of nanotubes	Lashmore, D.S., Lombard, C.	Nanocomp Technologies, Inc. (USA)

melt compounding of high-performance polymers such as polyetherimide of high melting point. Furthermore, the lack of electrical conductivity of clay platelets also limits their applications in functional electronic devices and sensors. In this regard, carbonaceous nanomaterials of very high aspect ratio, extraordinary high mechanical strength and stiffness, and superior electrical and thermal conductivity are excellent fillers for forming polymer nanocomposites with functional properties. The incorporation of these nanofillers into polymers improves their physical, mechanical, and thermal properties markedly. Such polymer nanocomposites show attractive applications as structural materials for bipolar plates of fuel cells, load-bearing materials for orthopedic implants, electromagnetic interference shielding materials, and functional materials for switching devices, chemical vapor sensors, and transducers.

Table 1.7 Manufacturers of carbonaceous nanomaterials.

Material	Manufacturer	Trade name	Web site information
Carbon nanotube	Carbon Solutions, Inc., USA	AP-SWNT; P2-SWNT P3-SWNT; P9-SWNT	*http://www.carbonsolution.com/*
Carbon nanotube	Carbon Nanotechnologies, Inc., USA	HiPCo	*http://www.cnanotech.com/*
Carbon nanotube	Nanoshel LLC, USA	Nanoshel™	*http://www.nanoshel.com/*
Carbon nanotube	Nanocyl S.A, Belgium	Nanocyl™ NC 7000 (MWNT)	*http://www.nanocyl.com/*
Carbon nanotube	Timesnano Company, China	TNM5, TNM7 (MWNT) TNS (SWNT)	*http://www.timesnano.com/*
Carbon nanotube yarn	Nanocomp Technologies, Inc., USA	C-Tex™	*http://www.nanocomptech.com/*
Carbon nanotube	Hanwha Nanotech Company, South Korea	ASA-100F (SWNT) CM-95 (MWNT)	*http://www.hanwhananotech.com/*
Carbon nanofiber	Applied Sciences, Inc., USA	Pyrograf® III	*http://www.apsci.com/*
Graphite nanoplatelet	XG Sciences, Inc., USA	xGnP	*http://www.xgsciences.com/*
Thermally reduced graphene oxide	Vorbeck Materials, Inc., USA	Vor-x™	*http://www.vorbeck.com/*

1.8.1
Composites with Carbon Black Nanoparticles

Carbon blacks (CBs) are colloidal, amorphous carbon particles with a distorted graphite structure [174, 175]. CBs are generally used as the reinforcements and conductive fillers for improving dimensional stability and imparting conductive behavior for rubbers and plastic products [176]. Furthermore, CB-filled polymer composites also find applications in electronic packaging and thermistor devices because of their cost advantage over other carbon-based fillers. In general, CBs can be classified into five types according to their manufacturing processes, that is, furnace black, thermal black, lamp black, channel black, and acetylene black. Among these, furnace black is the most commonly used and produced by thermal decomposition of aromatic oils in furnace reactors. This process yields CBs with diameters ranging from 10 to 100 nm and surface area from 25 to 1500 $m^2\,g^{-1}$. Thermal black is manufactured from natural gas feedstock in the furnace. The particle size, structure, and surface chemistry are three important characteristics of CBs for using as conductive fillers [177]. The CB morphology composes of prime particles fused into primary aggregates. The aggregate size, shape and the number of particles per aggregate determine the structure of CB. CBs with high surface area, high degree of porosity and elongated aggregates composing of prime particles with extensive branching (high-structure) can impart electrical conductivity at lower loadings in the polymer composites. However, such CBs are more expensive to produce. On the other hand, CBs with primary aggregates consist of relatively few prime particles, terming as the low structure, often yield large percolation threshold in the polymer composites. The structure of CBs can be evaluated from dibutyl phthalate (DBP) absorption test as described in the ASTM D2414-09a [178]. This test measures the amount of oil that can be absorbed by the CBs. A higher DBP value implies a higher structure of CB or vice versa. Balberg [179] indicated that the electrical conductivity of CB/polymer composites depends greatly on the CB structures. The percolation threshold of CB/PE (polyethylene) composites filled with high-structure CBs having a DBP value of 350 $cm^3/100\,g$ is 10 vol% while that of low-structure CBs with a DBP value of 43 $cm^3/100\,g$ is 39 vol%. The large filler contents in low-structure CB composites can cause high viscosity during processing and degrade mechanical performance of the composites markedly.

1.8.2
Composites with Graphene Oxide and Graphite Nanoplatelet Fillers

As aforementioned, rGO can be produced in large quantities via chemical reduction of GO colloidal dispersion. GO and rGO are inexpensive, versatile building blocks for carbon-based materials. GO can serve either as freestanding papers and thin films to form components of field-effect transistors, while rGO films can act as efficient electrical conductors for the sensors and electrodes in solar cells [180]. Functionalized rGO can be readily dispersed in a wide variety of polymers, this opens up tremendous opportunities for chemists and materials scientists to synthesize novel polymer nanocomposites with multifunctional properties at relatively low cost. The addition of low loadings of rGO and TRG into polymers can improve their electrical, mechanical, and thermal properties as well as dimensional stability significantly. Such nanocomposites find potential applications as electrode materials for batteries and ultracapacitors, hydrogen storage, electromagnetic interference shielding materials, automotive body panel, and so on. GNPs with diameters of 1–15 μm and thickness of <10 nm consist of a stack of multiple graphene sheets (Figure 1.14a,b). They possess smaller aspect ratio (width/thickness) than rGOs and TRGs as expected. Nevertheless, the incorporation of GNPs into polymers can produce mechanically strong and highly conductive polymer nanocomposites for the construction of bipolar plates in fuel cells and the electrodes for supercapacitors [181].

1.8.3
Composites with Carbon Nanotubes

CNT/polymer composites are characterized by high-strength, good electrical conductivity, very good thermal resistance and dimensional stability, and enhanced optical properties. The reinforcing effect of nanotubes in polymers renders them effective load-bearing materials for structural components of terrestrial, space and other engineering applications as well as human orthopedic implants. The excellent electrical conductivity of CNTs makes them suitable fillers for polymer nanocomposites that find useful applications in electronic and optoelectronic devices, coatings, electromagnetic interference shielding materials, actuators, chemical vapor sensors, and so on [182–186]. The most challenging issues for fabricating CNT-polymer nanocomposites are the high cost of CNTs, long processing time of purified nanotubes, and poor dispersion of nanotubes in the polymer matrix because of their high tendency for clustering.

Nomenclature

E	Young's modulus
e	Electronic charge
Go	Quantum electrical conductance
Goth	Quantum thermal conductance
h	Plank's constant
k_B	Boltzmann constant

References

1. Novoselov, K.S., Geim, A.K., Morozov, S., Jiang, D., Zhang, Y., Dubonos, S.V., Grigorieva, I.V., and Firsov, A.A. (2004) *Science*, **306**, 666–669.
2. Novoselov, K.S., Jiang, D., Schedin, F., Booth, T.J., Khotkevich, V.V., Morozov, S.V., and Geim, A.K. (2005) *Proc. Natl. Acad. Sci. U.S.A.*, **102**, 10451–10453.
3. Geim, A.K. and Novoselov, K.S. (2007) *Nat. Mater.*, **6**, 183–191.
4. Stankovich, S., Dikin, D.A., Dommett, G.H., Kohlhaas, K.M., Zimney, E.J., Stach, E.A., Piner, R.D., Nguyen, S.T., and Ruoff, R.S. (2006) *Nature*, **442**, 282–285.
5. Kim, H., Abdala, A.A., and Macosko, C.W. (2010) *Macromolecules*, **43**, 6515–6530.
6. Soldano, C., Mahmood, A., and Dujardin, E. (2010) *Carbon*, **48**, 2127–2150.
7. Lian, P., Zhu, X., Liang, X., Li, Z., Yang, W., and Wang, H. (2010) *Electrochem. Acta*, **55**, 3909–3914.
8. Berger, C., Song, Z.M., Li, X.B., Ogbazghi, A.Y., Feng, R., Dai, Z., Marchenkov, A.N., Conrad, E.H., First, P.N., and de Heer, W.A. (2004) *J. Phys. Chem. B*, **108**, 19912–19916.
9. Berger, C., Song, Z.M., Li, X.B., Wu, X.S., Brown, N., Naud, C., Mayo, D., Li, T.B., Hass, J., Marchenkov, A.N., Conrad, E.H., First, P.N., and de Heer, W.A. (2006) *Science*, **312**, 1191–1196.
10. Reina, F., Jia, X., Ho, H., Nezich, D., Son, H., Bulovich, V. Dresselhaus, M.S., and Kong, M.J. (2009) *Nano Lett.*, **9**, 30–35.

11. Kim, S.J., Zhao, Y., Jang, H., Lee, S.Y., Kim, J.M., Kim, K.S., Ahn, J.H., Kim, P., Choi, J.Y., and Hong, B.H. (2009) *Nature*, **457**, 706–710.
12. Li, X., Cai, W., An, J., Kim, S., Nah, J., Yang, D., Piner, R., Velamakanni, A., Jung, I., Tutuc, E., Barnejee, S.K., Colombo, L., and Ruoff, R.S. (2009) *Science*, **324**, 1312–1314.
13. Li, X.S., Cai, W.W., Colombo, L., and Ruoff, R.S. (2009) *Nano Lett.*, **9**, 4268–4272.
14. Zhao, L., Rim, K.T., Zhou, H., He, R., Heinz, T.F., Pinczuk, A., Flyn, G.W., and Pasupathy, A.N. (2011) *Solid State Commun.*, **151**, 509–513.
15. Shioyama, H. (2000) *Synth. Met.*, **114**, 1–15.
16. (a) Kim, H., Hahn, H.T., Viculis, L.M., Giljie, S., and Kaner, R.B. (2007) *Carbon*, **45**, 1578–1582; (b) Viculis, L.M., Mack, J.J., Mayer, O.M., Hahn, H.T., and Kaner, R.B. (2005) *J. Mater. Chem.*, **15**, 974–978.
17. (a) Chen, G.H., Wu, D.J., Weng, W.G., and Yan, W.L. (2001) *J. Appl. Polym. Sci.*, **82**, 2506–2513; (b) Chen, G.H., Weng, W., Wu, D., Wu, C., Lu, J., Wang, P., and Chen, X. (2004) *Carbon*, **42**, 753–759.
18. Celzard, A., Mareche, J.F., and Furdin, G. (2005) *Prog. Mater. Sci.*, **50**, 93–179.
19. Fukushima, H. (2003) Graphite reinforcements in polymer nanocomposites. PhD thesis. Michigan State University, East Lansing, MI.
20. Xiang, J.L. and Drzal, L.T. (2011) *Carbon*, **49**, 773–778.
21. Staudenmaier, L. (1898) *Ber. Dtsch. Chem. Ges.*, **31**, 1481–1487.
22. Hummers, W.S. and Offeman, R.E. (1958) *J. Am. Chem. Soc.*, **80**, 1339–1341.
23. Hontoria-Lucas, C., Lopez-Peinado, A.J., Lopez-Gonzalez, J., Rojas-Cervantes, M.L., and Martin-Aranda, R.M. (1995) *Carbon*, **33**, 1585–1592.
24. (a) He, H.Y., Klinowski, J., Forster, M., and Lerf, A. (1998) *Chem. Phys. Lett.*, **287**, 53–56; (b) Lerf, A., He, H.Y., Forster, M., and Klinowski, J. (1998) *J. Phys. Chem. B*, **102**, 4477–4482.
25. Park, S. and Ruoff, R.S. (2009) *Nat. Nanotechnol.*, **4**, 217–224.
26. Paredes, J.I., Villar-Rodil, S., Martinez-Alonso, A., and Tascon, J.M. (2008) *Langmuir*, **24**, 10560–10564.
27. Stankovich, S., Dikin, D.A., Piner, R.D., Kohlhaas, K.A., Kleinhammes, A., Jia, Y., Wu, Y., Nguyen, S.T., and Ruoff, R.S. (2007) *Carbon*, **45**, 1558–1565.
28. Eda, G. and Chhowalla, M. (2010) *Adv. Mater.*, **22**, 2392–2415.
29. Mattevi, C., Eda, G., Agnoli, S., Miller, S., Mkhoyan, K.A., Celik, O., Mastrogiovanni, D., Granozzi, C., Garfunkel, E., and Chhowalla, M. (2009) *Adv. Funct. Mater.*, **19**, 2577–2583.
30. Shin, H.J., Kim, K.K., Benayad, A., Yoon, S.M., Park, H.K., Jung, I.S., Jin, M.H., Jeong, H.K., Kim, J.M., Choi, J.Y., and Lee, Y.H. (2009) *Adv. Funct. Mater.*, **19**, 1987–1992.
31. Eda, G., Fanchini, G., and Chhowalla, M. (2008) *Nat. Nanotechnol.*, **3**, 270–274.
32. (a) Schniepp, H.C., Li, J.L., McAllister, M.J., Sai, H., Herrera-Alonso, M., Adamson, D.H., Car, R., Prud'homme, R.K., Saville, D.A., and Aksay, I.A. (2006) *J. Phys. Chem. B*, **110**, 8535–8539; (b) McAllister, M.J., Li, J.L., Adamson, D.H., Schniepp, H.C., Abdala, A.A., Liu, J., Herrera-Alonso, M., Milius, D.L., Car, R., Prud'homme, R.K., and Aksay, I.A. (2007) *Chem. Mater.*, **19**, 4396–4404.
33. Rafiee, M.A., Rafiee, J., Wang, Z., Song, H., Yu, Z.Z., and Koratkar, N. (2009) *ACS Nano*, **3**, 3884–3890.
34. Erickson, K., Erni, R., Lee, Z.H., Alem, N., Gannett, W., and Zettl, A. (2010) *Adv. Mater.*, **22**, 4467–4472.
35. Odom, T.W., Huang, J.L., Kim, P., and Lieber, C.M. (2000) *J. Phys. Chem. B*, **104**, 2794–2809.
36. Schnorr, J.M. and Swager, T.M. (2011) *Chem. Mater.*, **23**, 646–657.
37. Ebbesen, T.W. (1994) *Annu. Rev. Mater. Sci.*, **24**, 235–264.
38. Bystrzejewski, M., Rummeli, M.H., lange, H., Huczko, A., Baranowski, P., Gemming, T., and Pichler, T. (2008) *J. Nanosci. Nanotechnol.*, **8**, 6178–6186.

39. Ebbesen, T.W. and Ajayan, P.M. (1992) *Nature*, **358**, 220–222.
40. Zhao, X., Ohkohchi, M., Inoue, S., Suzuki, T., Kadoya, T., and Ando, Y. (2006) *Diamond Relat. Mater.*, **15**, 1098–1102.
41. Hou, P.X., Liu, C., and Cheng, H.M. (2008) *Carbon*, **46**, 2003–2025.
42. Zhao, X., Liu, Y., Inoue, S., Suzuki, T., Jones, R.O., and Ando, Y. (2004) *Phys. Rev. Lett.*, **92**, 125502.
43. Ando, Y. (2010) *J. Nanosci. Nanotechnol.*, **10**, 3726–3738.
44. Ando, Y., Zhao, X., Sugai, T., and Kumar, M. (2004) *Mater. Today*, **7**, 22–29.
45. Yudasaka, M., Yamada, R., Sensui, N., Wilkins, T., Ichihashi, T., and Iijima, S. (1999) *J. Phys. Chem. B*, **103**, 6224–6229.
46. Kusaba, M. and Tsunawaki, Y. (2006) *Thin Solid Films*, **506–507**, 255–258.
47. Muñoz, E., Maser, W.K., Benito, A.M., Martínez, M.T., de la Fuente, G.F., Righi, A., Anglaret, E., and Sauvajol, J.L. (2001) *Synth. Met.*, **121**, 1193–1194.
48. Rümmeli, M.H., Kramberger, C., Loeffler, M., Jost, O., Bystrzejewski, M., Gruneis, A., Gemming, T., Pompe, W., Buechner, B., and Pichler, T. (2007) *J. Phys. Chem. B*, **111**, 8234–8241.
49. Thess, A., Lee, R., Nikolaev, P., Dai, H., Petit, P., Robert, J., Xu, C., Lee, Y.H., Kim, S.G., Rinzler, A.G., Colbert, D.T., Scuseria, G.E., Tomanek, D., Fischer, J.E., and Smalley, R.E. (1996) *Science*, **273**, 483–487.
50. Yao, Y., Falk, L.K., Morjan, R.E., Nerushev, O.A., and Campbell, E.E. (2007) *Carbon*, **45**, 2065–2071.
51. Nessim, G.D., Seita, M., Plata, D.L., O'Brien, K.P., Hart, A.J., Reddy, C.M., Gschwend, P.M., and Thompson, C.V. (2011) *Carbon*, **49**, 804–810.
52. Bruden, B.A., Cassell, A.M., Ye, Q., and Meyyappan, M. (2003) *J. Appl. Phys.*, **94**, 4070–4078.
53. Jung, K.H., Shin, Y.S., Boo, J.H., Kim, Y.J., and Hong, B.Y. (2006) *Thin Solid Films*, **501**, 238–242.
54. Maschmann, M.R., Amama, P.B., Goyal, A., Iqbal, Z., and Fisher, T.S. (2006) *Carbon*, **44**, 10–18.
55. Fang, T.H., Chang, W.J., Lu, D.M., and Lien, W.C. (2007) *Appl. Surf. Sci.*, **253**, 8749–8753.
56. Garg, R.K., Kim, S.S., Hash, D.B., Gore, J.P., and Fisher, T.S. (2008) *J. Nanosci. Nanotechnol.*, **8**, 3068–3076.
57. Eres, G., Puretzky, A.A., Geohegan, D.B., and Cui, H. (2004) *Appl. Phys. Lett.*, **84**, 1759–1761.
58. Maschmann, M.R., Amama, P.B., Goyal, A., Iqbal, Z., and Fisher, T.S. (2006) *Carbon*, **44**, 2758–2763.
59. Hayashi, Y., Fukumura, T., Odani, K., Matsuba, T., and Utsonomiya, R. (2010) *Thin Solid Films*, **518**, 3506–3508.
60. Hiramatsu, M., Deguchi, T., Nagao, H., and Hori, M. (2007) *Diamond Relat. Mater.*, **16**, 1126–1130.
61. Levchenko, I., Ostrikov, K., and Keidar, M. (2008) *J. Nanosci. Nanotechnol.*, **8**, 6112–6122.
62. Meyyappan, M., Delzeit, L., Cassell, A., and Hash, D. (2003) *Plasma Sources Sci. Technol.*, **12**, 205–216.
63. Wong, W.K., Lee, C.S., and Lee, S.T. (2006) *J. Appl. Phys.*, **97**, 1871354 (6 pp).
64. Choi, K.S., Cho, Y.S., Hong, S.Y., Park, J.B., and Kim, D.J. (2001) *J. Eur. Ceram. Soc.*, **21**, 2095–2098.
65. Harutyunyan, A.R., Tokune, T., and Mora, E. (2005) *Appl. Phys. Lett.*, **87**, 051919 (3 pp).
66. Hu, J., Wang, O., and Lieber, C.M. (1999) *Acc. Chem. Res.*, **32**, 435–445.
67. Wu, Y. and Yang, P. (2001) *J. Am. Chem. Soc.*, **123**, 3165–3166.
68. Li, H., Shi, C., Du, X., He, C., Li, J., and Zhao, N. (2008) *Mater. Lett.*, **62**, 1472–1475.
69. Lee, C.J. and Park, J. (2001) *J. Phys. Chem. B*, **105**, 2365–2368.
70. Chen, X., Wang, R.M., Xu, J., and Yu, D.P. (2004) *Micron*, **35**, 455–460.
71. Nikolaev, P., Bronikowski, M.J., Bradley, R.K., Rohmund, F., Colbert, D.T., Smith, K.A., and Smalley, R.E. (1999) *Chem. Phys. Lett.*, **313**, 91–97.
72. Park, Y.S., Choi, Y.C., Kim, K.S., Chung, D.C., Bae, D.J., An, K.H., Lim, S.C., Zhu, X.Y., and Lee, Y.H. (2001) *Carbon*, **39**, 655–661.

73. Chiang, I.W., Brinson, B.E., Huang, A.Y., Willis, P.A., Bronikowski, M.J., Margrave, J.L., Smalley, R.E., and Hauge, R.H. (2001) *J. Phys. Chem. B*, **105**, 8297–8301.

74. Ebbesen, T.W., Ajayan, P.M., Hiura, H., and Tanigaki, K. (1994) *Nature*, **367**, 319–319.

75. Xu, Y.Q., Peng, H.Q., Hauge, R.H., and Smalley, R.E. (2005) *Nano Lett.*, **5**, 163–168.

76. Harutyunyan, A.R., Pradhan, B.K., Chang, J., Chen, G., and Eklund, P.C. (2002) *J. Phys. Chem. B*, **106**, 8671–8675.

77. Li, Y., Zhang, X.B., Luo, J.H., Huang, W.Z., Cheng, J.P., Luo, Z.Q., Li, T., Xu, G.L., Ke, X.X., Li, L., and Geise, H.J. (2004) *Nanotechnology*, **15**, 1645–1649.

78. Nepal, D., Kim, D.S., and Geckeler, K.E. (2005) *Carbon*, **43**, 660–662.

79. Ko, F.H., Lee, C.Y., Ko, C.J., and Chu, T.C. (2005) *Carbon*, **43**, 727–733.

80. Lu, K., Lago, R.M., Chen, Y.K., Green, M.L., Harris, P.J., and Tsang, S.C. (1996) *Carbon*, **34**, 814–816.

81. Andrews, R., Jacques, D., Qian, D., and Dickey, E.C. (2001) *Carbon*, **39**, 1681–1687.

82. Bonard, J.M., Stora, T., Salvetat, J.P., Maier, F., Stockli, T., Duschl, C., Forro, L., de Heer, W.A., and Chatelain, A. (1997) *Adv. Mater.*, **9**, 827–831.

83. Bandow, S., Rao, A.M., Williams, K.A., Thess, A., Smalley, R.E., and Eklund, P.C. (1999) *J. Phys. Chem. B*, **101**, 8839–8842.

84. Hu, H., Yu, A., Kim, E., Zhao, B., Itkis, M.E., Bekyarova, E., and Haddon, R.C. (2005) *J. Phys. Chem. B*, **109**, 11520–11524.

85. Yu, A., Bekyarova, E., Itkis, M.E., Fakhrutdinov, D., Webster, R., and Haddon, R.C. (2006) *J. Am. Chem. Soc.*, **128**, 9902–9908.

86. Vichchulada, P., Shim, J., and Lay, M.D. (2008) *J. Phys. Chem. C*, **112**, 19186–19192.

87. Mattia, D., Rossi, M.P., Kim, B.M., Korneva, G., Bau, H.H., and Gogotsi, Y. (2006) *J. Phys. Chem. B*, **110**, 9850–9855.

88. Yudasaka, M., Ichihashi, T., Kasuya, D., Kataura, H., and Iijima, S. (2003) *Carbon*, **41**, 1273–1280.

89. Nikolaev, P., Thess, A., Rinzler, A.G., Colbert, D.T., and Smalley, R.E. (1997) *Chem. Phys. Lett.*, **266**, 422.

90. Yudasaka, M., Kataura, H., Ichihashi, T., Qin, L.C., Kar, S., and Iijima, S. (2001) *Nano Lett.*, **1**, 487–489.

91. Arepalli, S., Nilolaev, P., Gorelik, O., Hadjiev, V.G., Holmes, W., Files, B., and Yowell, L. (2004) *Carbon*, **42**, 1783–1791.

92. Schweinberger, F.F., and Plath, A.M. (2011) *J. Phys. Conf. Ser.*, **304**, 012087 (10 pp).

93. Ferrari, A.C. and Robertson, J. (2000) *Phys. Rev. B*, **61**, 14095–140096.

94. Dresselhaus, M.S., Dresselhaus, G., Jorio, A., and Souza Filho, A.G. (2002) *Carbon*, **40**, 2043–2061.

95. Dillon, A.C., Parilla, P.A., Alleman, J.L., Gennett, T., Jones, K.M., and Heben, M.J. (2005) *Chem. Phys. Lett.*, **401**, 522–528.

96. Dillon, A.C., Yudasaka, M., and Dresselhaus, M.S. (2004) *J. Nanosci. Nanotechnol.*, **4**, 691–703.

97. Rao, A.M., Jorio, A., Pimenta, M.A., Dantas, M.S., Saito, R., Dresselhaus, G., and Dresselhaus, M.S. (2000) *Phys. Rev. Lett.*, **84**, 1820–1823.

98. Vigolo, B., Herold, C., Mareche, J.F., Ghanbaja, J., Gulas, M., Normand, F., Almairac, R., Alvarez, L., and Bantignies, J.L. (2010) *Carbon*, **48**, 949–963.

99. Wang, Y., Wu, J., and Fei, F. (2003) *Carbon*, **34**, 814–816.

100. Boccaleri, E., Arrais, A., Frache, A., Gianelli, W., Fino, P., and Camino, G. (2006) *Mater. Sci. Eng. B*, **131**, 72–82.

101. Ryabenko, A.G., Dorofeeva, T.V., and Zverera, G.I. (2004) *Carbon*, **42**, 1523–1535.

102. Itkis, M.E., Perea, D.E., Jung, R., Niyoki, S., and Haddon, R.C. (2005) *J. Am. Chem. Soc.*, **27**, 3439–3448.

103. Melechko, A.V., Merkulov, V.I., McKnight, T.E., Guillorn, M.A., Klein, K.L., Lowndes, D.H., and Simpson, M.L. (2005) *J. Appl. Phys.*, **97**, 41301 (39 pp)

104. Klein, K.L., Melechko, A.V., McKnight, T.E., Retterer, S.T., Rack, P.D., Fowlkes, J.D., Joy, D.C., and Simpson, M.L. (2008) *J. Appl. Phys.*, **103**, 061301 (6 pp).

105. Tibbets, G.G., Lake, M.L., Strong, K.L., and Rice, B.P. (2007) *Compos. Sci. Technol.*, **67**, 1709–1718.

106. Memon, M.O., Haillot, S., and Lafdi, K. (2011) *Carbon*, **49**, 3820–3828.

107. Miyagawa, H., Rich, M.J., and Drzal, L.T. (2006) *Thermochim. Acta*, **442**, 67–73.

108. Howe, J.Y., Tibbetts, G.G., Kwag, C., and Lake, M.L. (2001) *J. Mater. Res.*, **21**, 2646–2652.

109. Zhu, H., Li, X., Ci, L., Xu, C., Wu, D., Mao, Z. *et al.* (2003) *Mater. Chem. Phys.*, **78** (3), 670–675.

110. Endo, M., Kim, Y.A., Hayashi, T., Yanagisawa, T., Muramatsu, H., Ezaka, M., Terrones, H., Terrones, M., and Dresselhaus, M.S. (2003) *Carbon*, **41**, 1941–1947.

111. *http://www.apsci.com/*.

112. Odegard, G.M., Gates, T.S., Nicholson, L.M., and Wise, K.E. (2002) *Compos. Sci. Technol.*, **62**, 1869–1880.

113. Sakhaee-Pour A. (2009) *Solid State Commun.*, **149**, 91–95.

114. Liu, F., Ming, P.B., and Li, J. (2007) *Phys. Rev. B*, **76**, 064120 (7 pp).

115. Lu, Q. and Bhattacharya, B. (2005) *Eng. Fract. Mech.*, **72**, 2037–2071.

116. Tsai, J.L. and Tu, J.F. (2010) *Mater. Des.*, **31**, 194–199.

117. Jiang, J.W., Wang, J.S., and Li, B.W. (2009) *Phys. Rev. B*, **80**, 113405 (4 pp).

118. Khare, R., Mielke, S.L., Paci, J.T., Zhang, S., Ballarini, R., Schatz, G.C., and Belytschko, T. (2007) *Phys. Rev. B*, **75**, 075412 (12 pp).

119. Zheng, Q., Geng, Y., Wang, S., Li, Z., and Kim, J.K. (2010) *Carbon*, **48**, 4315–4322.

120. Lee, C.G., Wei, X.D., Kysar, J.W., and Hone, J. (2008) *Science*, **321**, 385–388.

121. Lee, C.G., Wei, X.D., Li, Q.Y., Carpick, R., Kysar, J.W., and Hone, J. (2009) *Phys. Status Solidi B*, **242**, 2562–2567.

122. Gomez-Navarro, C., Burghard, M., and Kern, K. (2008) *Nano Lett.*, **8**, 2045–2049.

123. Park, S.J., Lee, K.S., Bozoklu, G., Cai, W.W., Nguyen, S.B., and Ruoff, R.S. (2008) *ACS Nano*, **2**, 572–578.

124. *http://www.xgsciences.com/*.

125. Bolotin, K.I., Sikes, I.J., Jiang, Z., Klima, M., Fudenberg, G., Hone, J., Kim, P., and Stormer, H.L. (2008) *Solid State Commun.*, **146**, 351–355.

126. Du, X., Skachko, I., Barker, A., and Andrei, E.Y. (2008) *Nat. Nanotechnol.*, **3**, 491–495.

127. Chen, H., Muller, M.B., Gilmore, K.J., Wallace, G.D., and Li, D. (2008) *Adv. Mater.*, **20**, 3557–3561.

128. Park, S.J., An, J.H., Piner, R.D., Jung, I., Yang, D.X., Velamakanni, A., Nguyen, S.B., and Ruoff, R.S. (2008) *Chem. Mater.*, **20**, 6592–6594.

129. Schwamb, T., Burg, B.R., Schirmer, N.C., and Poulikakos, D. (2009) *Nanotechnology*, **20**, 405704 (5 pp).

130. Baladin, A.A., Ghosh, S., Bao, W., Calizo, I., Teweldebrhan, D., Miao, F., and Lau, C.N. (2008) *Nano Lett.*, **8**, 902–907.

131. Ghosh, S., Calizo, I., Teweldebrhan, D., Pokatilov, E.P., Nika, D.L., Baladin, A.A., Bao, W., Miao, F., and Lau, C.N. (2008) *Appl. Phys. Lett.*, **92**, 151911 (3 pp).

132. Seol, J.H., Jo, I.S., Moore, A.L., Lindsay, L., Aitken, Z.H., Pettes, M.T., Li, X.S., Yao, Z., Broido, D., Mingo, N., Ruoff, R.S., and Shi, L. (2010) *Science*, **328**, 213–216.

133. Yakobson, B.I., Brabec, C.J., and Bernholc, J. (1996) *Phys. Rev. Lett.*, **76**, 2511–2514.

134. Robertson, D.H., Brenner, D.W., and Mintmire, J.W. (1992) *Phys. Rev. B*, **45**, 12592–12595.

135. Yao, N. and Lordi, V. (1998) *J. Appl. Phys.*, **84**, 1939–1943.

136. Hernandez, E., Goze, C., Bernier, P., and Rubio, A. (1998) *Phys. Rev. Lett.*, **80**, 4502–4505.

137. Haskins, R.W., Maier, R.S., Ebeling, R.M., Marsh, C.P., Majure, D.L., Bednar, A.J., Welch, C.R., and Barker, B.C. (2007) *J. Chem. Phys.*, **127**, 074708 (10 pp).

138. Qin, Z., Qin, Q.H., and Feng, X.Q. (2008) *Phys. Lett. A*, **372**, 6661–6666.

139. Treacy, M.M., Ebbesen, T.W., and Gibson, J.W. (1996) *Nature*, **38**, 678–680.

140. Krishnan, A., Dujardin, E., and Ebbesen, T.W. (1998) *Phys. Rev. B*, **58**, 14013–14019.

141. Wong, E.W., Sheehan, P.E., and Lieber, C. (1997) *Science*, **277**, 1971–1975.

142. Salvetat, J.P., Kulik, A.J., Bonard, J.M., Briggs, A.D., Stockli, T., Metenier, K., Bonnamy, S., Beguin, F., Burnham, N.A., and Forro, L. (1999) *Adv. Mater.*, **11**, 61–65.

143. Yu, M.F., Lourie, O., Dyer, M.J., Kelly, T.F., and Ruoff, S. (2000) *Science*, **287**, 637–641.

144. Yu, M.F., Yakobson, B.I., and Rodney, S. (2000) *J. Phys. Chem. B*, **104**, 8764–8767.

145. Yu, M.F., Files, B.S., Arepalli, S., and Ruoff, S. (2000) *Phys. Rev. Lett.*, **84**, 5552–5555.

146. Demczyk, B.G., Wang, Y.M., Cumings, J., Hetman, M., Han, W., Zettl, A., and Ritchie, R.O. (2002) *Mater. Sci. Eng. A*, **334**, 173–178.

147. Lourie, O. and Wagner, H.D. (1998) *J. Mater. Res.*, **13**, 2418–2422.

148. Cooper, C.A., Young, R.J., and Harsall, M. (2001) *Composites Part A*, **32**, 401–411.

149. Yu, M.F. (2004) *J. Eng. Mater. Technol.*, **126**, 271–278.

150. Iijima, S., Brabec, C., Maiti, A., and Bernholc, J. (1996) *J. Chem. Phys.*, **104**, 2089–2092.

151. Falvo, M.R., Clary, G.J., Taylor, R.M., Chi, V., Brooks, J.P., Wasburn, S., and Superfine, B. (1997) *Nature*, **389**, 582–584.

152. Yakobson, B.I., Campbell, M.P., Brabec, C.J., and Bernholc, J. (1997) *Comput. Mater. Sci.*, **8**, 341–348.

153. Dereli, G. and Ozdogan, C. (2003) *Phys. Rev. B*, **67**, 0354161–0354166.

154. Huang, J.Y., Chen, S., Wang, Z.Q., Kempa, K., Wang, Y.M., Jo, S.H., Chen, G., Dresselhaus, M.S., and Ren, Z.F. (2006) *Nature*, **439**, 281–281.

155. Fischer, J.E., Dai, H., Thess, A., Lee, R., Hajani, N.M., Dehaas, D.L., and Smalley, R.E. (1997) *Phys. Rev. B*, **55**, R4921–R4924.

156. Bockrath, M., Cobden, D.H., McEun, P.L., Chopra, N.G., Zettl, A., Thess, A., and Smalley, R.E. (1997) *Science*, **275**, 1922–1925.

157. Ebbesen, T.W., Lezec, H.J., Hiura, H., Bennett, J.W., Ghaemi, H.F., and Thio, T. (1996) *Nature*, **382**, 54–56.

158. Sanvito, S., Kwon, Y.K., Tomanek, D., and Lambert, C.L. (2000) *Phys. Rev. Lett.*, **84**, 1974–1977.

159. Frank, S., Poncharal, P., Wang, Z.I., and de Heer, W.A. (1998) *Science*, **280**, 1744–1746.

160. Berber, S., Kwon, Y.K., and Tománek, D. (2000) *Phys. Rev. Lett.*, **84**, 4613–4616.

161. Osman, M.A. and Srivastave, D. (2001) *Nanotechnology*, **12**, 21–24.

162. Schwab, K., Henriksen, E.A., Worlock, J.M., and Roukes, M.L. (2000) *Nature*, **404**, 974–976.

163. Mingo, N. and Broido, D.A. (2005) *Phys. Rev. Lett.*, **95**, 096105 (4 pp).

164. Hone, J., Whitney, M., Piskoti, C., and Zettl, A. (1999) *Phys. Rev. B*, **59**, R2514–R2516.

165. Kim, P., Shi, L., Majumdar, A., and McEuen, P.L. (2001) *Phys. Rev. Lett.*, **87**, 215502 (4 pp).

166. Fuji, M., Zhang, X., Xie, H., Ago, H., Takahashi, K., Ikuta, T., Abe, H., and Shimizu, T. (2005) *Phys. Rev. Lett.*, **95**, 065502 (4 pp).

167. Pop, E., Mann, D., Wang, Q., Goodson, K., and Dai, H. (2006) *Nano Lett.*, **6**, 96–199.

168. Yi, W., Lu, L., Zhang, D.L., Pan, Z.W., and Xie, S.S. (1999) *Phys. Rev. B*, **59**, R9015–R9018.

169. Prasher, R. (2008) *Phys. Rev. B*, **77**, 075424 (11 pp).

170. Ozkan, T., Naraghi, M., and Chasiotis, I. (2010) *Carbon*, **48**, 239–244.

171. Tjong, S.C., Meng, Y.Z., and Hay, A.S. (2002) *Chem. Mater.*, **14**, 44–51.

172. Tjong, S.C. and Mai, Y.W. (2010) *Physical Properties and Applications of Polymer Nanocomposites*, Woodhead Publishing, Oxford.

173. Vanderhart, D.L., Asano, A., and Gilman, J.W. (2001) *Chem. Mater.*, **13**, 3796–3809.

174. Bourrat, X. (1993) *Carbon*, **31**, 288–300.

175. Donnet, J.B. (1994) *Carbon*, **32**, 1305–1310.

176. *http://carbon-black.org/*.

177. Huang, J.C. (2002) *Adv. Polym. Technol.*, **21**, 299–313.

178. ASTM (2009) D2414-09a. *Standard Test Method for Carbon Black: Oil Absorption Number (OAN)*, American Society for Testing and Materials, West Conshohocken, PA.

179. Balberg, I. (2002) *Carbon*, **40**, 139–143.

180. Compton, O.C. and Nguyen, S.B. (2010) *Small*, **6**, 711–723.

181. Zhamu, A. and Jang, B.Z. (2011) Process for producing nano-scaled graphene platelet nanocomposites electrodes for supercapacitors. U.S. patent 7875219.

182. Park, C., Watson, K.A., Ounaies, Z., Connell, J.W., Smith, J.G., and Harrison, J.S. (2009) Electrically conductive, optically transparent polymer/carbon nanotube composites and process for preparation thereof. U.S. patent 7588699.

183. Harmont, J.P. and Clayton, L.M. (2008) Polymer/carbon nanotube composites, methods of use and methods of synthesis thereof. U.S. patent 7399794.

184. Zhao, Y.P., Chen, Y.C., Zhang, X.C., Raravikar, N.R., Ajayan, P.M., Lu, T.M., Wang, G.C., and Schadler, L.S. (2004) Ultrafast all-optical switch using carbon nanotube polymer composites. U.S. patent 6782154.

185. Terai, M., Hasegawa, M., Okusawa, M., Otani, S., and Oshima, C. (1998) *Appl. Surf. Sci.*, **130–132**, 876–882.

186. Geohegan, D.B., Ivanov, I.N., Puretzky, A.A., Jesse, S., Hu, B., Garrett, M., and Zhao, B. (2011) Transparent conductive nanocomposites. U.S. patent 7923922.